

**Theory of magnetic 3d transition metal dopants in gallium nitride**Peter A. Schultz <sup>\*</sup>*Sandia National Laboratories, Albuquerque, New Mexico 87185, USA*

Arthur H. Edwards

*Space Vehicles Directorate, Air Force Research Laboratory, Kirtland AFB, New Mexico 87117, USA*

Renee M. Van Ginhoven

*Directed Energy Directorate, Air Force Research Laboratory, Kirtland AFB, New Mexico 87117, USA*

Harold P. Hjalmarson and Andrew M. Mounce

*Sandia National Laboratories, Albuquerque, New Mexico 87185, USA* (Received 13 December 2022; revised 1 March 2023; accepted 13 April 2023; published 11 May 2023)

Using first-principles density functional theory (DFT) methods and size-converged supercell models, we analyze the electronic and atomic structure of magnetic 3d transition metal dopants in cubic gallium nitride (c-GaN). All stable defect charge states for Fermi levels across the full experimental gap are computed using a method that correctly resolves the boundary condition problem (without a jellium approximation) and eliminates finite-size errors. The resulting computed defect levels are not impacted by the DFT band-gap problem, they span a width consistent with the experimental gap rather than being limited to the single-particle DFT gap. All defects with electronically degenerate (half-metal)  $T_d$  ground states are found to have significant distortions, relaxing to  $D_{2d}$  structures driven by the Jahn-Teller instability. This leads to insulating ground states for all substitutional 3d dopants, refuting claims in the literature that  $+U$  or hybrid functional methods are required to avoid artificial half-metal results. Interpreting the  $d^n$  atomic occupations within a crystal-field model and exchange splittings, we identify a systematic trend across the 3d transition metal series. Approaches to estimate excited-state energies as observed in photoluminescence from defect centers are assessed, ranging from a Koopmans-type single-particle energy interpretation to relaxed total energy differences in fully self-consistent DFT. The single-particle interpretations are found to be qualitatively predictive and the calculations are consistent with the limited available experimental data across the 3d dopant series. These results provide a baseline understanding to guide future studies and a conceptual framework within which to interpret new results.

DOI: [10.1103/PhysRevB.107.205202](https://doi.org/10.1103/PhysRevB.107.205202)**I. INTRODUCTION**

Wide band-gap semiconductors such as gallium nitride (GaN) have revolutionized solid state lighting (e.g., blue LEDs), and show immense promise for other optoelectronic applications. Successfully harnessing the greater temperature tolerance, faster switching speeds, and larger breakdown voltages that might be possible with III-nitrides would profoundly improve the efficiency and performance of power electronics. To realize this significant potential requires a greater fundamental understanding of the behavior of atomic defects that govern the behavior of the material, be they dopants intention-

ally introduced to achieve a desired functionality or undesired impurities and structural defects that degrade performance.

Doping GaN with 3d transition metals can be used to create dilute magnetic semiconductors (DMS), of potential value for novel spintronic applications [1]. The transition metals introduce localized 3d states in the band gap. These localized  $d$ -electron spins on the 3d dopant atoms tend to align to form durable magnetic moments with high Curie temperatures, above room temperature, that can then possibly be exploited in practical device applications. The  $d$  orbitals of 3d dopants create localized spin states that might be manipulated optically, making these attractive candidates for applications in quantum information science. The  $\text{Cr}^{4+}$  in GaN (and SiC) has proven to be one such promising candidate [2], and Zn-doped GaN also exhibits a prominent photoluminescence center [3]. The search continues for other optically active defect centers with improved properties and ease of manufacture. However, the discovery and design of new candidate optical centers is limited by a lack of basic understanding of the optical and magnetic properties of 3d defects in GaN. There exists only a rudimentary and largely incomplete description of the basic

<sup>\*</sup>Corresponding author: paschul@sandia.gov

electronic properties of  $3d$  dopants, either in experiment or theory; often not even the stable charge states or defect levels are known with any confidence.

In this paper, we perform a systematic computational analysis of isolated transition metal dopants in cubic GaN across the  $3d$  series using size-converged, large-scale, first-principles density functional theory (DFT) calculations. To accurately describe the charged-supercell boundary conditions, we use the local moment counter-charge (LMCC) method to avoid the errors inherent to a jellium neutralization. We assess and verify elimination of finite-supercell-size errors to obtain bulk-converged results. We adopt a generalized gradient approximation (GGA) [4] rather than a local density approximation (LDA) because spin and magnetism are an important discriminating aspect of transition metal dopants. GGA generally can be expected to perform better for magnetic  $3d$  metals than LDA. We identify all the stable charge states as a function of the Fermi level (defect levels) across a full experimental band gap, unhindered by a band-gap problem. The intentional structural optimizations systematically investigate possible symmetry-lowering distortions for defects vulnerable to Jahn-Teller instabilities. Knowledge of the electronic properties of defects in GaN is primarily embodied in a wealth of experimental photoluminescence data in GaN [5] that is mostly chemically undifferentiated, with few reliable assignments to specific defect centers. We characterize the electronic structure and analyze the trend of the  $d$  occupancies and spin states for  $3d$  dopants across the  $3d$  series, and do a systematic survey of potential viable electronic excited states accessible via intrasite ( $d$ -to- $d$ ) transitions that might lead to photoluminescence (PL). Full total energy DFT calculations are shown to give good estimates of PL excitations for the limited data that are available. A simplistic approach, a Koopmans-type interpretation using differences in GGA single-particle energies, is discovered to be qualitatively, and even semiquantitatively, predictive, particularly after taking into account the typical magnitude of electronic self-consistency and structural relaxation obtained in those calculations where total energy DFT calculations are possible. These results provide a baseline understanding of ground-state  $3d$  dopant defect structure in GaN, which should be useful in the analysis of optical measurements probing excited states in  $3d$ -doped GaN.

## II. BACKGROUND AND CONCEPTUAL FRAMEWORK

In contrast to medium band-gap systems such as Si or GaAs, direct experimental data concerning charge transition energies (defect levels) in the gap or defect chemical structure in GaN are scant. Defect identifications using the chemically undifferentiated PL spectra are very challenging, and characterization of ground-state structures with first-principles calculations can be invaluable in deciphering the available experimental data and identifying chemical defect structures. An early computational study from Gerstmann *et al.* [6] surveyed Sc through Cu substituted for Ga in the zinc-blende structure cubic gallium nitride (c-GaN). This pioneering analysis used small computational models and the local density approximation (LDA) within a Green's function method that precluded consideration of atomic relaxation, but computed the electronic structure and defect levels with sufficient fidelity to

provide valuable preliminary insight toward interpreting results from PL and PL excitation spectra in III-nitrides.

Other early LDA calculations targeting GaN:Mn<sub>Ga</sub> [7–10] did find localized majority-spin  $d$ -electron states in the band gap. The neutral Mn defect calculations led to a half-metal state: the minority-spin band structure was insulating, but the Fermi level was pinned to a partially occupied majority-spin  $3d$  defect band. This half-metal behavior was found in both cubic GaN (c-GaN) or wurtzite structure (w-GaN), and reported to persist even upon augmenting the LDA functional with a Hubbard  $+U$  model [8,9].

These studies, however, did not consider symmetry-lowering structural distortions around the dopant. Wolos *et al.* [11] had inferred from their magneto-optical experiments that the neutral Mn dopant in c-GaN, vulnerable to a symmetry-lowering structural distortion due to its electronic ground-state degeneracy, indeed led to a Jahn-Teller (JT) distortion favored by 37 meV. This distortion would open a gap between the occupied and unoccupied majority-spin states, creating a semi-insulating ground state. This conclusion was confirmed in later XANES (x-ray absorption near edge structure) experiments reported by Smolentsev *et al.* [12]. The nature of the symmetry distortion around c-GaN:Mn<sub>Ga</sub>(0) was specifically determined to be from symmetric  $T_d$  to a tetragonally distorted  $D_{2d}$  structure. Calculations from Boguslawski and Bernholc [10] found large atomic relaxations from bulk crystal positions in w-GaN, but only small JT distortions. Using a generalized gradient approximation functional, Luo and Martin [13] reported more significant distortions, finding a  $D_{2d}$  structure to be 0.10 eV lower than the mixed-occupation  $T_d$  structure.

Stroppa and Kresse [14] claimed that hybrid functionals, replacing a portion of density functional exchange with explicit Hartree-Fock exchange, were necessary to obtain the JT distorted semi-insulating ground state for the neutral Mn dopant. Virost *et al.* obtained a JT distortion in LDA  $+U$  calculations (lowering by 38 meV) [15], similarly asserting that a beyond-DFT method was necessary to obtain the correct semi-insulating structure. These broad assertions concerning the failure of standard local DFT functionals had already been undermined by the finding of JT distortions in the generalized gradient approximation (GGA) results from Luo and Marti [13]. The comparative analyses from Volnianska *et al.* [16] and Zakrzewski *et al.* [17] additionally showed that changes in the computed electronic structure caused by these extensions beyond DFT led to inconsistencies with optical measurements in Mn-doped GaN, i.e., hybrid functionals and  $+U$  methods worsened comparisons to experiment.

The salient features of the electronic structure within the  $3d$  dopant series are most fruitfully interpreted as incremental occupation of the  $3d$  shell within crystal-field theory. A  $3d$  transition metal atom substitutes for the Ga atom in the lattice, as illustrated in Fig. 1. The five  $d$  orbitals of a transition metal  $M$ , degenerate in the free atom, are split into a tripleton  $t_2$  and a (lower-energy) doubleton  $e$  manifold when substituted into the Ga site in (cubic) c-GaN. For greater clarity [to differentiate orbital degeneracy from the spin degeneracy (a central quantity for  $3d$  dopants)] we reserve below the singlet, doublet, triplet, etc., terminology strictly to specify spin multiplicity and use singleton, doubleton, tripleton, etc., to differentiate orbital degeneracies. In the wurtzite structure,

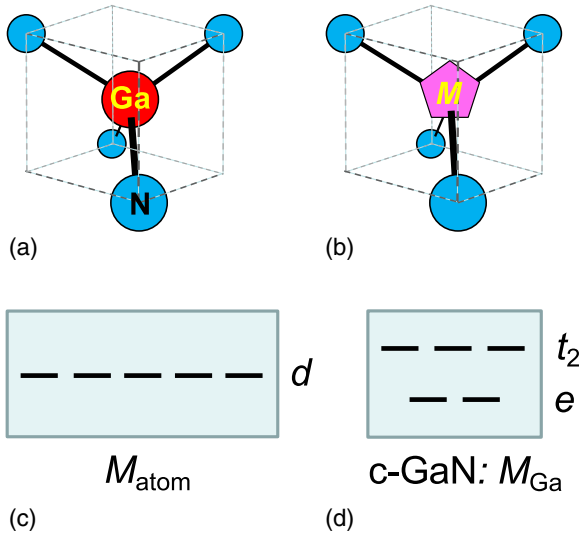


FIG. 1. The local geometric and electronic structure of a  $3d$  dopant  $M$  in cubic-GaN. (a) The Ga site in the crystal lattice bonds to four nitrogen atoms in tetrahedral directions. (b) The  $3d$  transition metal atom  $M$  replaces the Ga atom in the lattice. Three of the dopant atom electrons go toward filling the Ga contributions to the Ga–N bonds, which are embedded within the occupied valance bands. The crystal field splits the (c) fivefold  $d$ -orbital degeneracy (in the free atom) into a (d)  $t_2$  triplet above an  $e$  doublet when substituted into the Ga site in the c-GaN lattice.

this local environment is not exactly tetrahedral, but distortion from a local  $T_d$  in the a Ga–N bond along the threefold axis is only a minor perturbation to this triplet-doubleton description in c-GaN. See the analysis by Wolos *et al.* [11] for a particularly accessible description of the sequential energy level structure descending from crystal-field theory, using the example of the  $Mn^{+3}(0) d^4$  ion.

Three of the  $3d$  dopant atom electrons replace the absent Ga valence electrons in bonds to the neighboring N atoms. These electrons embed within the valence band, composed of the Ga–N bond network. Hence, a nominal  $M^{+3}$  oxidation state is the default for a neutral  $M_{Ga}(0)$  dopant. This atomic oxidation state is not a system charge state, and in the following we will avoid this convention in favor of the more determinate overall system charge state. We will discuss the atomic dopant structure in terms of the occupations of the  $d$ -electron orbitals, from which more meaningful trends across the series of  $3d$  dopants can be elicited.

The  $3d$  dopant transition series is characterized by the incremental occupation of the split  $t_2$  and  $e$  manifolds. With three electrons devoted to fill the bond to the neighbors, the first  $3d$  dopant, the first  $d$ -orbital occupation, is with the Ti atom, and the final transition dopant is Zn. The  $d^{10}$  shell is definitively filled and electronically inert with an unsubstituted Ga. This simplistic model is largely borne out in the calculations we present below.

With strong exchange coupling between the relatively localized  $3d$  states, the  $d$  electrons in the undistorted  $T_d$  structure in Fig. 1 tend to occupy the degenerate manifolds according to Hund’s rule. First the spin-up (majority-spin) orbitals within a degenerate manifold fill in a high-spin

configuration, and then later electrons fill the spin-down (minority-spin) to incrementally reduce the total spin. A question we carefully probe is whether and when the exchange splitting is exceeded by the crystal-field orbital splitting, and whether the electrons fill the spin-up orbitals through the higher  $t_2$  triplet before filling the spin-down orbitals in the lower  $e$  doublet. The crystal-field splitting becomes dominant in later  $3d$  dopants: occupying the crystal-field stabilized  $e^\downarrow$  becomes favored over the exchange-stabilized  $t_2^\uparrow$ , closing the  $e$  shell before again adding spin-up electrons into a high-spin  $t_2$  triplet.

An additional important consideration is potential symmetry-lowering structural distortions ensuing from a Jahn-Teller instability in a degenerate electronic ground state in the symmetric  $T_d$  structure. A partial filling of a spin manifold (either a single electron or hole in the  $e$  doublet, or one or two electrons or holes in the  $t_2$  triplet) leads to partial orbital occupations and an overall degenerate electronic state. In principle, according to the Jahn-Teller theorem, a structural distortion can couple to this degeneracy, leading to a lower-energy ground state that removes the degeneracy.

In practice, the presence of a JT instability does not predict the sense of the likely distortion, nor does it predict its magnitude. In their calculations, Virot *et al.* [15] reported only a tiny 0.7-meV JT distortion in the  $Mn_{Ga}(0)$  defect using a LDA, physically meaningless at room temperature, which increased to a more substantial 38 meV in a LDA +  $U$  treatment. The magnitude of the distortion and the temperature of a measurement will determine whether this manifests as a static distortion or as a dynamic JT that appears to be symmetric. Our analysis will not investigate this distinction between static and dynamic JT effects.

### III. COMPUTATIONAL METHODS

The defect calculations are executed with the SEQUEST density functional theory (DFT) code [18], within a supercell computational model [19]. With spin polarization and magnetism being an important figure of merit in these transition metal dopants, the first-principles calculations use the Perdew-Burke-Ernzerhof (PBE) flavor of the generalized gradient approximation [4] as the form of the exchange-correlation potential describing the electron-electron interactions. Select calculations are also done with the local density approximation as parametrized by Perdew and Zunger [20]. The correct asymptotic electrostatic boundary conditions in the supercells for systems with net charge are enforced with the use of the local moment countercharge method to solve the Poisson equation [21,22], avoiding the errors ensuing from the conventional jellium neutralization. Using a method for computed defect levels founded upon the LMCC, we obtained an average accuracy of 0.1 eV in comparison to a large number of known defect levels in silicon, defect level energies known experimentally [23], an accuracy that was replicated in GaAs [24,25] for its fewer number of experimentally known defects.

The atomic pseudopotentials (PP) are taken from the SEQUEST library. The PP used in this study were generated using the FHI98PP code [26] with custom parametrizations optimized to maximize chemical transferability [27]. The nitrogen PP was generated within a Troullier-Martins form and

TABLE I. Construction of  $3d$  transition metal pseudopotentials. All  $3d$  PP were built using the FHI98PP code [26] using these custom settings, optimized to maximize transferability. All reference atomic calculations were performed in a singly ionized state (+1), with the indicated valence orbital occupations. The angular momentum potentials were either in the Hamann (H) form [30] or the Troullier-Martin (TM) form [32], using the radial parameter indicated, in the Bohr atomic units native to the PP code, and also added a nonlinear partial core correction [33] with the matching radius shown. The  $d$  potential was used as the local potential in  $l_{\max} = 2$  pseudopotentials in all cases, except the  $3d$ -core Ga potential, where a “hard”  $4f$  potential ( $R_f = 1.2$ ) was added to the pseudopotential to serve as the local potential.

Element	$Z_{\text{valence}}$	Atomic valence	Pseudopotential settings				
			$R_{\text{NLCC}}$	$3p^6$	$3d$	$4s$	$4p$
Sc	9	$3p^6 3d^1 4s^1 (+1)$	0.6	H (0.58)	H (0.43)	H (1.72)	
Ti	10	$3p^6 3d^2 4s^1 (+1)$	0.6	H (0.53)	H (0.38)	H (1.64)	
V	11	$3p^6 3d^3 4s^1 (+1)$	0.6	H (0.50)	H (0.33)	H (1.53)	
Cr	12	$3p^6 3d^4 4s^1 (+1)$	0.6	TM 1.50	TM 1.50	H 1.40	
Mn	7	$3d^5 4s^1 (+1)$	0.6	(Core)	TM 1.50	H 1.32	H 1.32 <sup>a</sup>
Fe	8	$3d^6 4s^1 (+1)$	0.6	(Core)	TM 1.50	H 1.30	TM 2.50
Co	9	$3d^7 4s^1 (+1)$	0.6	(Core)	TM 1.50	H 1.19	TM 2.55
Ni	10	$3d^8 4s^1 (+1)$	0.6	(Core)	TM 1.50	H 1.15	TM 2.38
Cu	11	$3d^{9.5} 4s^{0.5} (+1)$	(None)	(Core)	TM 1.50	H 1.11	TM 2.35
Zn	12	$3d^{10} 4s^1 (+1)$	(None)	(Core)	TM 1.50	H 1.04	H 1.15
Ga <sup>b</sup>	3	$4s^{1.5} 4p^{0.5} (+1)$	1.6	(Core)	H 2.05(4d)	H 1.10	H 1.04

<sup>a</sup>The Mn  $4p$  pseudopotential additionally set the linearization energy to 0.01 eV.

<sup>b</sup>Adds a  $4f$  potential with  $R_f = 1.2$  bohrs, to act as a sufficiently “hard” local potential.

uses the  $p$  potential as the local potential. The gallium atom represents a particularly difficult challenge for PP construction for DFT calculations [28]. It is computationally expensive to include the semicore  $3d^{10}$  as valence electrons, but it is non-trivial to design and verify a viable, chemically transferable PP that buries the  $3d$  shell into the core shells of the PP. In recent work, we discovered that a  $d^{10}$ -core and  $d^{10}$ -valence PP gave similar results for defect levels for intrinsic defects [29]. The  $d^{10}$ -core PP gave slightly better results, attributed to its better agreement with the c-GaN lattice constant, 4.482 Å, compared to experiment, 4.52(5) Å. Hence, we adopt the more computationally economical  $3d$ -core Ga PP, in a Hamann-type generalized norm-conserving form [30], for our defect calculations.

The formulation of the PP across the  $3d$  transition metal series is summarized in Table I. As for the Ga, these  $3d$  atom pseudopotentials were generated with the FHI98PP code [26], with particular attention paid to converging spin properties. As prescribed in the DFT primer [27] results using these PP were converged with respect to the PP parameters, verified against available full-potential all-electron results in the literature, and validated in frequent usage, including a recent investigation of  $3d$  transition metal dopants in 4H-SiC [31]. That study also found that results using PBE-LMCC mostly matched jellium-based hybrid functional results; where there were significant differences the PBE-LMCC compared as well or more favorably to available experiment.

### A. LMCC-based approach for defect levels without jellium

In this section we provide a concise primer for the method used for computing accurate defect levels in finite supercell calculations of charged defects avoiding the errors of the jellium approximation [23]. The primary step is to eliminate the standard jellium approximation with the use of a self-consistent LMCC approach to rigorously impose the correct

electrostatic boundary condition in the solution of the Poisson equation for charged defects in finite supercells [21,22]. With this method, the potential energy for the addition or removal of electron charge is exactly fixed for all defect calculation, that is mathematically equivalent to asymptotically aligning the potential of every charged defect calculation to the perfect crystal potential at infinite distance [22].

The energy contribution from long-range screening of the dielectric outside the volume of the supercell is computed via a modified Jost model [23]. This Jost screening term is described in greater detail by Schultz *et al.* in a study of defects in 3C-SiC [34]. The modified Jost screening model we use here is described in our earlier paper on intrinsic defects in GaN [29]. The long-range screening model uses the experimental dielectric constant (9.5), and an unscreened skin depth [23,34] of 1.2 bohrs. This provides good convergence to a bulk limit for the calculated defect level energies, verified in calculations from 64- up to 1000-atom supercells to eliminate finite-cell-size errors due to electrostatics. We confirm this model in the calculations presented below for the  $3d$  dopant defects.

The defect ionization potentials are calculated in the usual way, as differences in these total energies between defects of different charge, to obtain ionization energies across all defects [23]. We emphasize that the Kohn-Sham (KS) eigenvalues do not enter into this total energy calculation at any point, they are strictly used only to confirm that every defect calculation has its defect KS eigenstates within the KS gap. We note that a defect eigenstate that occupies a conduction band edge (CBE) state, or deoccupies a valence band edge (VBE) state, is not a viable localized state, and is rejected as a viable local defect. The use of the more rigorous charge boundary conditions of the LMCC (as opposed to the standard jellium approximations) defines a common electron chemical potential for all charge transitions, so that a spectrum of computed defect ionization potentials shares a common (but unknown)

crystal reference [23]. The reference is equivalent to aligning the electrostatic potentials for charged and neutral defects to be equal infinitely far from the defect, a bulk reference analogous to the vacuum reference used for molecular systems. This referencing does not predict the position of the band edges in this spectrum of computed ionization potentials [23].

The final step to create the defect level diagram is to recalibrate the ionization potential spectrum from the crystal reference to a band reference (i.e., infer the position of the band edges on this computed defect ionization spectrum). The energies of the band edges cannot be computed within an equivalent theory: the LMCC is strictly applicable to localized defect charge and band states are not localized; and conversely, the KS eigenvalues are not valid descriptors of total energies [35,36]. However, we can use the span of computed defect levels (each verified to be with the KS gap) to define practical bounds on the positions of the CBE and VBE with respect to this computed defect level spectrum. The highest computed ionization energy bounds the conduction band edge position from below, while the lowest computed ionization energy bounds the valence band edge position from above. These bounds then define an effective defect band gap (EDBG). Defect levels so computed have been shown in Si to provide accuracy (cf. experiment) of 0.1–0.2 eV across the full band gap despite a formal KS band-gap problem [23]. The computed defect level diagrams for GaAs exhibit this accuracy across a full band gap and are shown to provide an effective defect band gap in agreement with the experimental gap (1.5 eV). The effective band gap is largely insensitive to the KS band gap, ranging from 0.1–1.1 eV in GaAs (depending on the functional and pseudopotentials) [24,37]. The computed defect levels prove accurate enough to (re)assign defect identifications on the strength of the computed defect levels [25].

The process above was applied for c-GaN defects in our previous work [29]. Once again, the computed defect levels proved insensitive to a KS band-gap problem, for either choice of large ( $Z = 3$  or “ $d0$ ”) and small ( $Z = 13$  or “ $d10$ ”) pseudopotentials. The experimental band gap for (metastable) zinc-blende structure GaN had been determined to be 3.30 eV [38] while that for the (ground-state) wurtzite structure is 3.50 eV [39]. For the Ga( $d0$ ) pseudopotentials used in this study, the effective defect band gap (EDBG) was determined to be  $\sim 3.5$  eV [29] despite a KS band gap of 2.4 eV [28]. We note that the Ga( $d10$ ) pseudopotentials had generated very similar defect levels and a comparable effective defect band gap, despite a smaller KS band gap of 1.5 eV. In the following, we note that all density of states (DOS) plots, intended to discriminate the behavior of the localized and (presumptively) nondispersive defect states, use the states at the  $k$  sampling used in the total energy DFT calculation (not over the full Brillouin zone). In this work, the results restricted to the  $3d$  defects alone provide a comparable effective gap, confirming the previous analysis over intrinsic defects [29].

## B. Supercells and structure

The methods for the defect calculations herein follow the approach used in an earlier comprehensive analysis of intrinsic defects in c-GaN [29], to which we refer the reader for

greater details of the computational setup and their validation for c-GaN. Foreshadowing the assessment here, those PBE defect results in GaN, with proper treatment of the boundary condition problem, provide defect level results that avoid a band-gap problem.

To assess the convergence to a bulk limit and verify the elimination of finite-size errors, we perform the calculations for c-GaN in a series of cubic supercells ranging in size up to 1000 atoms. A  $T_d$  local symmetry allows for discriminating and highly resolved tests of the local electronic structure and resulting Jahn-Teller distortions for the  $3d$  dopants and facilitates direct comparisons to previous work for GaN dating back to the pioneering work of, e.g., Gerstmann *et al.* [6]. The close similarity of defects in cubic and wurtzite GaN had been noted long ago by Van de Walle and Neugebauer [40] and this similarity was confirmed in our recent comprehensive study of intrinsic defects in GaN [29].

We exhaustively search for stable candidate (integer) charge states for each defect, keep those where the defect Kohn-Sham (KS) eigenstates lie within the KS band gap, and dismiss as unstable those where a conduction (valence) band edge eigenstate is (de)occupied. Similarly, the spin state for a given defect in a given charge is also systematically explored, within the constraint of discrete total spin states consistent with the electron number, i.e., for defects with an odd number of electrons, we investigate spin polarization constrained to total spin  $S = \frac{1}{2}, \frac{3}{2}, \frac{5}{2}, \dots$  and constrained to  $S = 0, 1, 2, \dots$  for defects with an even number of electrons. The determination of a stable spin state uses the same criterion as for the charge state: the KS eigenvalues for both the majority- and minority-spin single-particle states must lie within the KS band gap.

The supercell models are constructed as  $N \times N \times N$  scaling of the conventional eight-atom cubic unit cell, with an optimized PBE lattice constant at 4.484 Å (in LDA, 4.390 Å). The results reported here are from  $4 \times 4 \times 4$  512-atom supercells, all confirmed to be converged (usually within  $< 20$  meV) in comparison to  $3 \times 3 \times 3$  216-atom supercells. For comparison to earlier literature, select results are obtained in small  $2 \times 2 \times 2$  (64-atom) supercells, and in several cases the calculations are extended to  $5 \times 5 \times 5$  1000-atom supercells to achieve and demonstrate cell-size convergence. The integral over the Brillouin zone is approximated by a discrete sampling of a regular  $2 \times 2 \times 2$   $k$  grid, offset from  $\Gamma$ , except for the small 64-atom supercell, where a  $3^3$   $k$  grid is needed to converge the calculation.

The supercell lattice constant is fixed to the theoretical value, and all the atoms within the cell are relaxed to their equilibrium ground-state positions, deemed converged when the forces on each atom are less than 0.0002 Ry/bohrs (5 meV/Å). This ensured total energies numerically converge to within 1 meV of the ground state, less than the 0.01 eV quoted for defect levels in this work, and much less than the  $O(0.1)$  eV physical accuracy that (optimistically) can be expected within the DFT approximation.

## C. Electronic excitations

The DFT is only formally valid for the electronic ground-state density in a given charge state and total spin. For

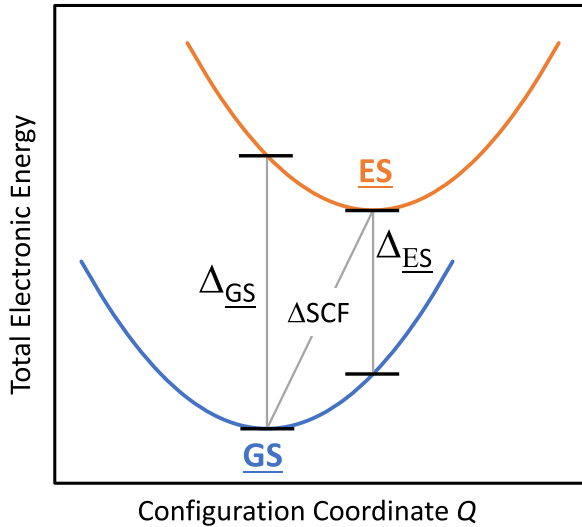


FIG. 2. Idealized configuration coordinate diagram describing the potential energy surface along a lattice coordinate  $Q$  for the ground-state electronic state and excited-state electronic state. The  $\Delta\text{SCF}$  represents the difference between the fully relaxed structures  $\text{GS}$  and  $\text{ES}$ ,  $\Delta\text{GS}$  is the vertical excitation energy to the ES computed in the  $\text{GS}$  structure, and  $\Delta\text{ES}$  is the vertical excitation energy computed in the  $\text{ES}$  structure.

excitations that change the total spin state, such as in a spin-flip excitation, the excitation energy can often be computed as a  $\Delta\text{SCF}$ . This  $\Delta\text{SCF}$  is the difference between the relaxed DFT energy of the defect in two different total spin states, the ground state  $\text{GS}$  and the excited state  $\text{ES}$ , as illustrated in the configuration coordinate diagram in Fig. 2. The vertical transition energies between the  $\text{GS}$  in the  $\text{GS}$  structure and the  $\text{ES}$  in the  $\text{ES}$  structure,  $\Delta\text{GS}$  excitation from the  $\text{GS}$  structure and  $\Delta\text{ES}$  (de)excitation from the  $\text{ES}$  structure, are defined in this diagram.

A spin-conserving excitation occupies a single-particle orbital above an empty single-particle orbital. This violates the DFT ansatz and the direct calculation of the excitation energy as the difference between DFT total energies is not possible in standard DFT theory. Although Sham and Kohn cautioned against interpreting DFT single-particle eigenvalues and eigenstates as physical quantities [35], a Koopmans-type interpretation of the single-particle energies is often very useful. Figure 3 presents a single-particle energy diagram and illustrates how to estimate excitation energies  $\Delta\epsilon$  as differences in single-particle energies between the occupied state and empty state involved in the promotion of an electron. In the following, we assess the quality of this  $\Delta\epsilon$  estimate of the excitation energy to the corresponding (electronically relaxed)  $\Delta\text{GS}$  and  $\Delta\text{ES}$  and the full (structurally relaxed)  $\Delta\text{SCF}$  for the spin-flipped excitations, before discussing these  $\Delta\epsilon$  estimates for the spin-conserving excitations for which a  $\Delta\text{SCF}$  computed between standard ground-state DFT calculations is not possible.

#### IV. RESULTS AND ANALYSIS

The Mn dopant has been a frequent subject of computational studies of  $3d$  dopants in GaN. We begin our analysis of  $3d$  dopants in GaN with Mn, partly in an attempt to reconcile

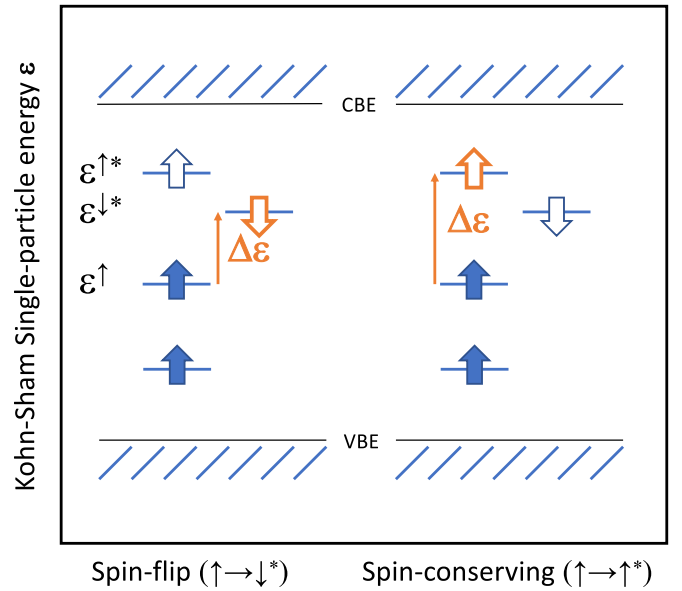


FIG. 3. Approximating excited-state energies as Koopmans-type differences in  $d \rightarrow d$  single-particle eigenenergies  $\Delta\epsilon$ . The energy to excite from an occupied spin-up single-particle state with eigenenergy  $\epsilon^\uparrow$  to an empty spin-down state with  $\epsilon^{\downarrow*}$  in a spin-flip excitation is estimated by  $\Delta\epsilon = \epsilon^{\downarrow*} - \epsilon^\uparrow$ . The energy of a spin-conserving excitation is given as the difference in eigenenergies of the occupied spin-up and the empty spin-up state the electron is promoted into:  $\Delta\epsilon = \epsilon^{\uparrow*} - \epsilon^\uparrow$ . A spin-flip excitation can be addressed in a standard DFT  $\Delta\text{SCF}$  calculation, while a spin-conserving excitation cannot, as the excited state leaves an empty eigenstate below an occupied state.

conflicting conclusions from these earlier works, but primarily to motivate the computational framework used in this study in this detailed example before launching into a more expansive discussion of results over the full transition metal dopant series.

It is well established that  $3d$  atoms such as Mn preferentially substitute for a Ga atom in the GaN lattice, as described in the computational study of Cui *et al.* [41]. Our calculations confirm this strong preference for the chemically expected Ga site (by more than 5 eV). The following results consider only a single  $3d$  dopant atom substituted for a Ga atom in the c-GaN lattice.

##### A. $\text{Mn}_{\text{Ga}}$ dopant

The neutral Mn dopant devotes three electrons to the Ga-N bonds, leaving four electrons to be distributed into its  $d$  orbitals. The permitted spin states are a low-spin singlet with a full  $e$  manifold (two spin up, two spin down), a triplet upon promotion of a  $e^\downarrow$  into a  $t_2^\uparrow$  orbital, and a high-spin quintet with upon promotion of the last  $e^\downarrow$ . Consistent with the observation that Mn doping leads to a dilute magnetic semiconductor, the high-spin quintet is the ground state, favored over the triplet by 1.14 eV and over the singlet by 1.01 eV (constrained to a  $T_d$  structure). The exchange coupling dominates over the crystal-field orbital splitting.

Reflecting the greater antibonding character in the  $t_2$ -triplet  $d$  orbitals ( $xy, yx, zx$ ) vs the nonbonding  $e$ -doubleton

( $x^2-y^2$ ,  $3z^2-r^2$ )  $d$  orbitals, the Mn–N distance length contracts 1.9% (cf. the Ga–N bond) in the singlet, contracts by only 0.4% in the triplet (with one  $t_2$  electron), and then lengthens by 1.9% in the quintet (with its two  $t_2$  electrons). The  $d$  electrons are strongly localized, but nonetheless interact sufficiently with the neighboring nitrogen to influence the bonding.

The singlet is a nondegenerate total state, with a fully occupied  $e$  shell and no  $t_2$  electrons. The high-spin states have partial occupancies of the  $t_2$  triplet and therefore represent a degenerate total state. Presence of this overall degeneracy signals a half-metallic state (the Fermi level coincides with the orbital degeneracy) but also indicates a vulnerability to a symmetry-lowering structural distortion via a Jahn-Teller instability.

In our calculations, we explore incremental symmetry lowerings from the cubic  $T_d$  along two paths: the tetragonal  $D_{2d}$  distortion and the trigonal  $C_{3v}$  distortion. The trigonal distortions (both elongating or shortening the Mn–N bond along the  $C_{3v}$  threefold symmetry axis) prove uncompetitive in every defect we examined. In the JT-vulnerable Mn(0) and Mn(1+) states, the lowering was  $<20$  meV. We ignore trigonal distortions henceforward. It is worth noting that this  $C_{3v}$  distortion would correspond to the change in the native local environment in going from the cubic to the wurtzite structure of GaN. This result suggests that local pairing and resonant distortions dominate over trigonal distortions, and in wurtzite GaN it might be insufficient to depend upon the local trigonal symmetry to accurately resolve JT instabilities.

A tetragonal  $D_{2d}$  distortion can take two senses, as illustrated in Fig. 4: a pairing- $D_{2d}$  ( $-pD_{2d}$ ) structure that elongates along the tetragonal axis and N-atom pairs approach each other, and a compression along the tetragonal axis in a “resonant”- $D_{2d}$  ( $-rD_{2d}$ ) structure. This distinction proves useful to classify and understand the nature of the JT distortions around  $M_{\text{Ga}}$  in terms of the crystal-field-split single-particle level structure. The  $pD_{2d}$  distortion splits the  $t_2$  triplet, lowering a singleton state below a degenerate doubleton, while the  $rD_{2d}$  distortion does the reverse, splitting a doubleton below a singleton. If the incremental symmetry lowering from  $T_d$  must result in a nondegenerate final state, then this differentiated splitting predicts the preferred sense of the  $D_{2d}$  distortion. Both senses split the  $e$  doubleton into nondegenerate singletons. We also considered a second-stage distortion from a JT-vulnerable degenerate  $D_{2d}$  to a  $C_{2v}$ , and in every case, we found these to collapse back to the  $D_{2d}$  ground state (nondegenerate) structure, i.e., no further symmetry lowering was obtained. Lacking either a degeneracy to indicate a JT instability, or a chemically inspired directional bonding that might induce a symmetry lowering, no other lower-symmetry structures were considered in these calculations.

The Jahn-Teller distortion energies for Mn<sub>Ga</sub>, here defined as the difference in total energy of the relaxed ground-state  $D_{2d}$  structure with respect to the relaxed  $T_d$  structure, are presented in Table II. In accordance with the simple bonding model depicted in Fig. 4, an  $rD_{2d}$ , with nominally two high-spin electrons in the  $t_2$ , is the ground state for the neutral Mn dopant. This  $rD_{2d}$  structure has a JT lowering of almost 0.1 eV, and agrees with the determination from XANES experiments [12]. The opposite sense, to give a  $pD_{2d}$ , yields a degenerate total electronic state and  $<20$  meV lowering. The quartet

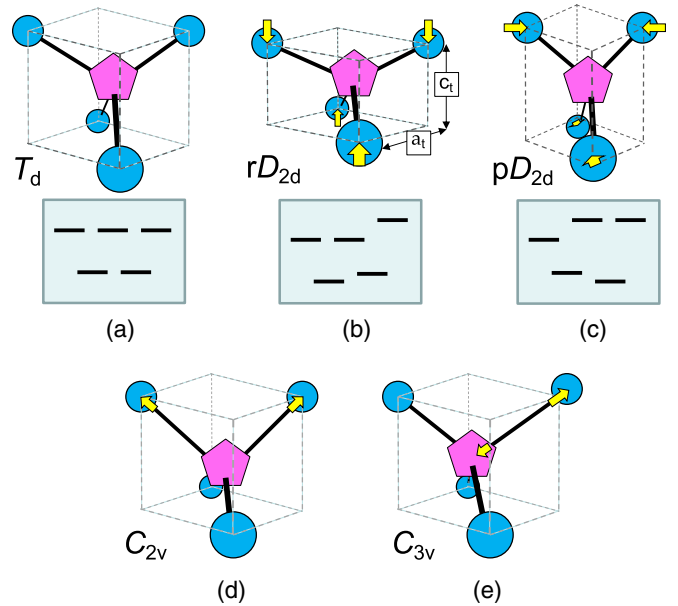


FIG. 4. Structural distortions and splittings of  $d$ -shell single-particle levels. (a) The high-symmetry  $T_d$  structure has a triplet  $t_2$  above a doubleton  $e$ . A tetragonal  $D_{2d}$  distortion splits both the triplet  $t_2$  and doubleton  $e$ . (b) The resonant- $D_{2d}$  structure brings a doubleton below a singleton in the  $t_2$ , while (c) the pairing- $D_{2d}$  structure brings a singleton below the doubleton. This  $d$ -orbital level structure dictates the sense of the distortions in the  $3d$  dopant defects. We also considered a further lowering of  $D_{2d}$  to (d)  $C_{2v}$  to split the remaining doubleton degeneracy, which was never found to lead to lowering from a  $D_{2d}$  and an alternate trigonal distortion to (e) a  $C_{3v}$  structure, which yielded energy lowerings that were much smaller than tetragonal  $D_{2d}$  distortions.

ground state for the Mn(1+) has only one  $t_2$  electron and reverses this order, favoring a  $pD_{2d}$  ground state with a JT lowering also nearly 0.1 eV.

These results contradict assertions in the literature that local DFT cannot correctly predict a distortion unless embellished with an empirical  $+U$  to approximately remove self-interaction errors [15], or mixing in an empirical portion of explicit Hartree-Fock exchange in a hybrid functional [14]. The extended results presented in Table II offer possible rationalizations for this contrast. Early studies [7–10,15] frequently employed LDA functionals. A GGA such as PBE [4] with its improved accuracy for spin localization and mag-

TABLE II. Jahn-Teller distortion energies for ground-state structures for the Mn(0) and Mn(1+) dopants, as a function of supercell size and functional. These  $\Delta E_{\text{JT}}$  are computed as the difference between the total energies of the fully relaxed structures in the  $T_d$  and the lowest-energy  $D_{2d}$  structure, in meV.

$\Delta E_{\text{JT}}$ (meV)	Mn(0)- $rD_{2d}$		Mn(1+)- $pD_{2d}$	
	LDA	PBE	LDA	PBE
Supercell				
( $2 \times 2 \times 2$ )	-13	-36	-10	-31
( $3 \times 3 \times 3$ )	-48	-74	-54	-79
( $4 \times 4 \times 4$ )	-53	-80	-66	-94

TABLE III. Structure of Jahn-Teller distortions for ground-state structure for the Mn charged defects ( $4 \times 4 \times 4$  cells). The tetragonal distortion ratio  $c_t/a_t$  (as defined in Fig. 4) [36], the Mn–N bond length, and distances between the four N neighbors (two “pairing” and four “resonant” distances) (all in Å).

	Mn(1–) $T_d$	Mn(0) $rD_{2d}$	Mn(1+) $pD_{2d}$	Mn(2+) $T_d$
$c_t/a_t$	1.0	0.939	1.068	1.0
$R(\text{Mn–N})$ (Å)	2.053	1.974	1.897	1.821
$R(\text{N–N})$ pair(2)	3.352	3.290	3.028	2.973
$R(\text{N–N})$ res(4)	3.352	3.190	3.132	2.973

netism in 3d metals is more advisable. We observe that our LDA results indeed lead to weaker distortions than the PBE. Previous results using GGA functionals by Luo and Martin [13], and Stroppa and Kresse [14] had found significant JT distortions (by 0.10 eV, and unspecified, respectively). We additionally find a strong dependence on supercell size. The net JT distortion energy is reduced in the small 64-atom supercells, and reduced even more significantly in the LDA. This decreased margin might be somewhat misleading about

the strength of the distortion. This increasing JT distortion energy is primarily due to the cell-size error in the  $T_d$  calculation. The formation energy of the distorted  $D_{2d}$  structure is largely insensitive (within  $\sim 5$  meV) to supercell size, but this nonetheless helps explain why early studies, computationally limited to small supercells, experienced difficulties in finding significant JT distortion energies for  $\text{Mn}_{\text{Ga}}$ . The triplet excited state of the  $\text{Mn}_{\text{Ga}}(0)$  described as a  $t_2^\uparrow \rightarrow e^\downarrow$  excitation from the ground-state quintet exhibits a JT distortion surpassing 0.2 eV in its fully relaxed  $pD_{2d}$  ground-state structure.

Table III summarizes the local structural distortions around the Mn dopant site in its different charge states, and quantitatively presents the nature of the distortions depicted in Fig. 4. The four equivalent Mn–N bonds get progressively shorter as additional electrons are removed. The  $D_{2d}$  distortion is reflected in the tetragonal compression or expansion in the cage defined by the four N neighbors, succinctly characterized via the tetragonal distortion ratio  $c_t/a_t$  [using the  $c_t$  and  $a_t$  defined in Fig. 4(b)] [36]. The symmetric  $T_d$  structure has an ideal distortion ratio of one, the  $pD_{2d}$  has  $c_t/a_t$  greater than one (with two N–N pair distances less than four N–N resonant distances), while the  $rD_{2d}$  has  $c_t/a_t$  less than one (and two N–N pair distances greater than the four N–N resonant

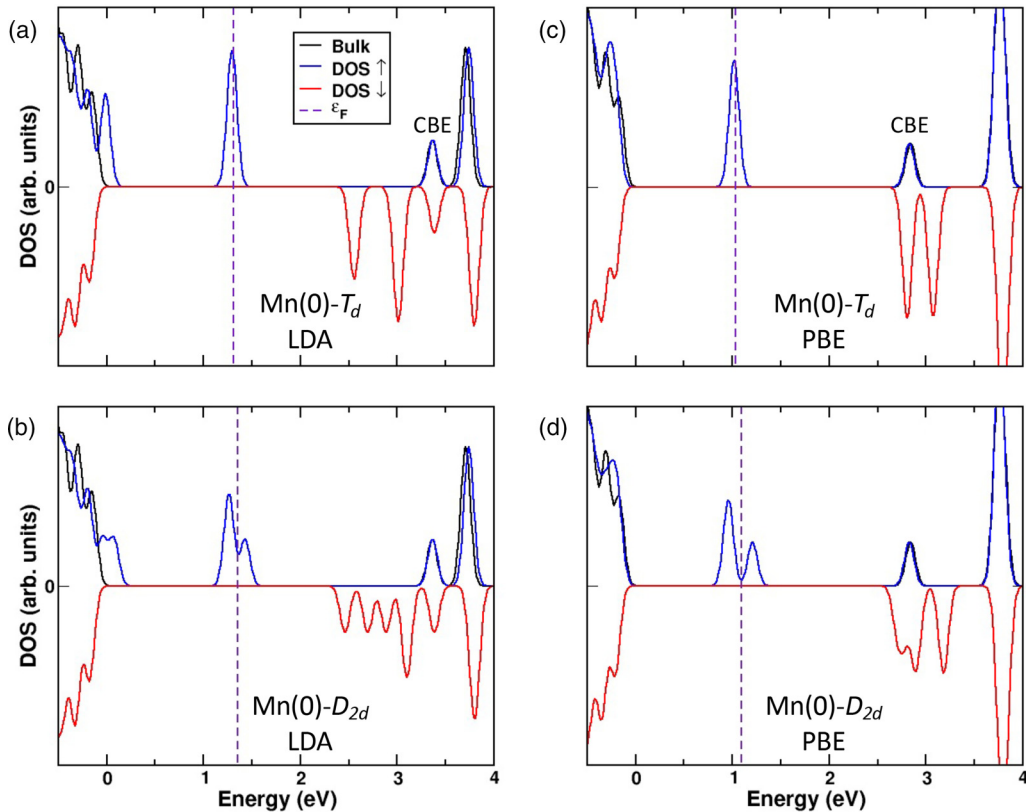


FIG. 5. The projected density of states for the neutral  $\text{Mn}_{\text{Ga}}$  (216-atom supercell), showing the opening of a gap upon relaxation from the symmetric  $T_d$  structure to the tetragonally distorted  $D_{2d}$  structure: (a) LDA  $T_d$ ; (b) LDA  $D_{2d}$ ; (c) PBE  $T_d$ ; (d) PBE  $D_{2d}$ . A partially occupied  $t_2$  triplet splits into an occupied triplet-spin doublet below an unoccupied singleton, converting a half-metallic defect into an insulating state, in both the GGA and in the LDA approximations. In close quantitative agreement with the computed PBE band structure of Stroppa and Kresse [their Fig. 1(a)] [14], the occupied  $e$ -defect band is right at the VBE, while this partially occupied  $t_2$  defect band is  $\sim 1$  eV above the band edge. The perfect crystal DOS is drawn in solid black, mostly overlaid by the defect DOS, the near perfect alignment of the crystal and defect bulk DOS testifying to the degree of localization of the defect states in the gap.

distances). As expected from the crystal-field analysis of the  $d$ -shell splittings, the Mn(1−) and Mn(2+) retain a symmetric  $T_d$  structure, while the intervening Mn(0) undergoes a significant Jahn-Teller–driven distortion to a  $rD_{2d}$  structure and the Mn(1+) undergoes a significant  $pD_{2d}$  distortion.

The projected density of states in Fig. 5 depicts the physical consequence of this distortion for Mn(0). In the  $T_d$  structure, the Fermi level passes through the partially occupied majority-spin  $t_2$  triplet, a conducting spin channel that implies a half-metal. Upon distortion, the  $t_2$  triplet splits: the Fermi level passes in the gap between the occupied doublet and empty singleton, creating an insulating state. The distortion also splits the unoccupied minority-spin single-particle states. In the LDA, these states are in the KS gap and both the  $e$  doublet and  $t_2$  triplet split by more than 0.2 eV. In the PBE, the empty minority-spin states are above the CBE marker state, but can nonetheless be cleanly resolved and the degeneracy is also broken upon distortion.

The Mn(1−) defect has five local  $d$  electrons and is established in EPR (electron paramagnetic resonance) experiments to be a high-spin sextet ( ${}^6A_1$ ) ground state [42] and inferred that the Mn(0) and Mn(1+) were JT distorted. Our calculations obtain this  $T_d$  sextet as the ground-state structure for Mn(1−): one up-spin electron sits in each of three degenerate  $t_2$  orbitals and an up-spin electron sits in each  $e$  orbital. This ( $t_2^\uparrow t_2^\uparrow t_2^\uparrow e^\uparrow e^\uparrow$ ) state occupation can be depicted in the shorthand ( $\uparrow \uparrow \uparrow \uparrow \uparrow \uparrow$ ).

The sextet Mn(1−) is a nondegenerate electronic ground state and no symmetry-lowering distortion is anticipated. Neither of the other permitted spin states are stable in these PBE calculations. The ( $\uparrow \uparrow o \mid \uparrow \downarrow \uparrow$ ) spin-quartet calculation fails to bring the requisite empty  $e^\downarrow$  below the CBE. The ( $\uparrow o o \mid \uparrow \downarrow \uparrow \downarrow$ ) spin-doublet succeeds in bringing the spin-up and -down  $e$  orbitals below the CBE, but the now-filled  $e$  shell pushes the occupied  $t_2^\uparrow$  orbital above the CBE.

Korotkov *et al.* [43] had tentatively attributed a PL band at 1.25 eV to a quartet-sextet transition in the Mn(1−), apparently at odds with this result. Their assignment might have been too speculative, but this result would nonetheless be within the anticipated limits of the accuracy of the DFT: we find the missing  $e^\downarrow$  eigenstate needed to stabilize the quartet is less than 0.25 eV above the Kohn-Sham CBE. Zakrzewski *et al.* [17] had instead ascribed the transition to the  $e^\downarrow \rightarrow t_2^\uparrow$  transition in the Mn(0). Our quintet-triplet total energy difference  $\Delta\text{SCF}$  for the Mn(0) gives a result of 1.0 eV, which would underestimate this PL measurement by 0.25 eV. The variance in these different results indicates that assignment of these PL lines remains inconclusive.

In the Mn(1+), the other permitted (doublet) spin state is computed to be 0.26 eV higher than the high-spin quartet ground state (in the  $T_d$  structure). This difference is significant enough to overwhelm any plausible JT distortion energy. The Mn(1+) quartet ground state distorts to a  $pD_{2d}$  structure, with an energy lowering from the  $T_d$ ,  $\Delta E_{\text{JT}}$ , of almost 0.1 eV (Table II).

In these calculations, we find that the Mn dopant can donate yet another electron, to form a Mn(2+). The resulting triplet-coupled electrons fill the majority-spin  $e$  doublet and this Mn(2+) retains a  $T_d$  structure. This doublet sinks below

the Kohn-Sham VBE, so that no additional electrons can be ionized.

Figure 6 depicts the stable charge states and resulting charge transition defect levels for Mn<sub>Ga</sub>. The computed PBE-LMCC thermodynamic Mn(1−/0) defect level sits at VBE+2.04 eV, consistent with measurements of the (1−/0) acceptor state in experiments [42,44,45]. This agrees with the (1−/0) acceptor level quoted by Stroppa and Kresse using a hybrid functional (VBE+1.9), but is significantly higher than their reported PBE result (VBE+1.6) [14]. That discrepancy in the PBE values can be attributed to finite-size supercell errors and their primitive (jellium-based) treatment of the charge boundary conditions. The current results are cell-size converged and use the more rigorous LMCC boundary conditions. Whether, or by how much, these finite-size errors might impact their quoted HSE value is unknown.

Korotkov *et al.* had ascribed a PL peak at 1.42 eV to the (1−/0) charge transition [45]. This PL peak would align better with our computed (0/1+) transition. Graf *et al.* [42] argued compellingly that this PL should instead be assigned to an intrasite excitation.

Han *et al.* observed a charge transition at VBE+1.1 eV, which they attributed to the (0/1+) donor state [46]. Our Mn(0/1+) defect level is predicted to lie 1.46 eV above the VBE and a Mn(1+/2+) defect level at +1.11 eV. Stroppa and Kresse did not report finding any donor level in their calculations [14], while Gerstmann *et al.* found a single-donor state. A second donor (1+/2+) transition was only ever mentioned by Boguslawski and Bernholc [10] [we note that a single-particle level structure presented by Zakrzewski *et al.* [17] depicted an occupied  $t_2$  state in the gap for the Mn(1+) that would, in principle, imply a stable doubly ionized defect]. The existence of this (1+/2+) level is predicted here with high confidence: our computed (1+/2+) level is nearer midgap than the band edge. This is well outside the largest error seen using the PBE-LMCC approach to date. The transition level at VB+1.1 eV reported by Han *et al.* [46] and attributed to the (0/1+) transition would instead align very well with our calculated (1+/2+) transition and be <0.3 eV less than our computed (0/1+). Given a lack of unambiguous discriminating data, and lack of systematic validation to confidently determine the accuracy of DFT predictions vs experimental observations in GaN, it is not possible to make a definitive assignment on the basis of these results and existing experimental data. GaN:Mn, despite an extensive published history, needs further and more targeted investigations.

## B. The 3d dopant transition series

In this section we shift to discuss the behavior in the wider series of 3d transition metal dopants for which there is even less conclusive knowledge in existing literature than for Mn. We begin with a discussion of the ground-state structures of the stable charge states and their defect levels, and then continue with an extensive assessment of methods to estimate excitation energies within the DFT calculations.

### 1. Defect levels and structure

Figure 7 shows the computed defect levels for the 3d dopants  $M_{\text{Ga}}$ . The results indicate that the 3d transition metal

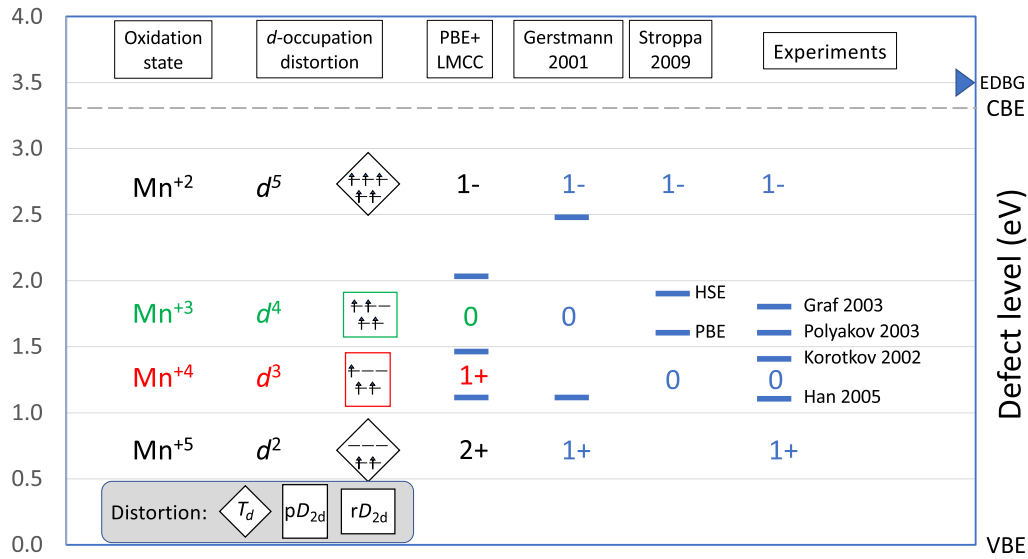


FIG. 6. The stable charge states with their electronic and structural configurations and charge transition defect levels in the gap for the Mn<sub>Ga</sub> dopant. The results are compared to levels computed in previous theory (Gerstmann [6], Stroppa [14]) and also to various (1−/0) levels (Graf [42], Polyakov [44], and Korotkov [45]) and a (0/1+) level (Han [46]) quoted in experimental studies. Gerstmann quoted both an acceptor and donor level in their calculations [6] while Stroppa only reported an acceptor level [14] (both using the HSE and using the PBE functional). The current calculations additionally predict the existence of a double-donor (2+) state with a (1+/2+) defect level at 1.1 eV. (Color used solely to help guide the eye along a particular  $d^n$  configuration through a sequence of atoms.) The CBE is marked by a dashed line at the experimental band gap and the position of the effective defect band gap is marked by the triangle.

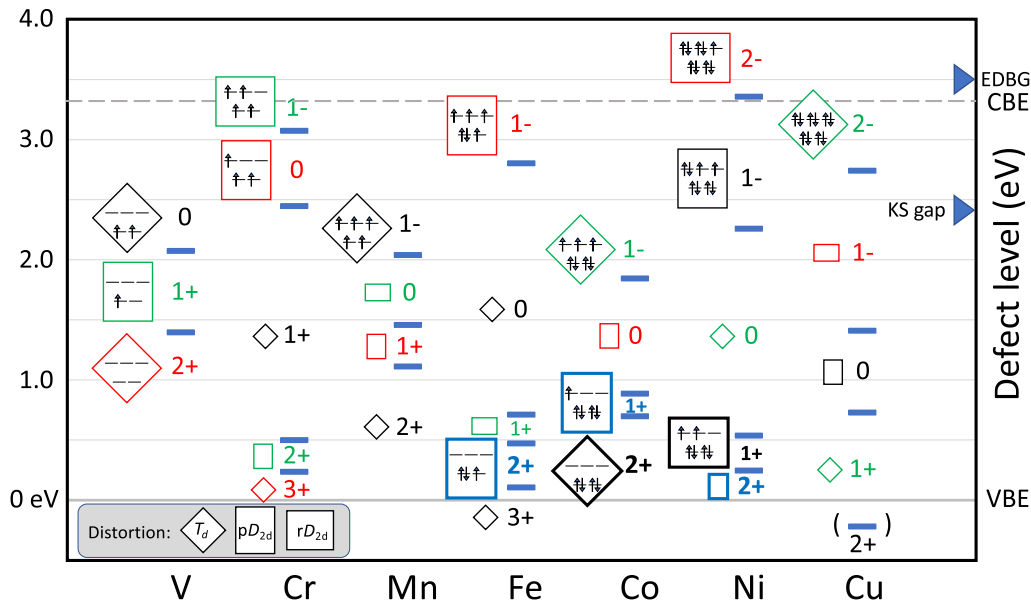


FIG. 7. Predicted PBE-LMCC electronic structure and defect levels for magnetic 3d dopants in c-GaN. The magnetic 3d dopants are bounded at one end by titanium, which proves to be a shallow donor, and at the other end by zinc, which is a shallow acceptor. In the limit of a  $T_d$  structure, the distribution of the defect  $d$  electrons into the  $t_2$  and  $e$  states is shown. Those state occupations enclosed in diamonds are nondegenerate ground states and remain  $T_d$ . The tall rectangles denote a distortion to a paired- $D_{2d}$  structure, and the wide rectangles denote a distortion to a resonant- $D_{2d}$  structure. Color is used solely to help guide the eye along a particular  $d^n$  configuration through a sequence of atoms, e.g., the Cr(1+), Mn(2+), and Fe(3+) share the same occupation distortion as the V(0). The CBE is marked by a dashed line at the experimental band gap (3.3 eV), the position of the effective defect band gap ( $\sim 3.5$  eV) is marked, and the extent of the (physically meaningless) Kohn-Sham gap (2.40 eV) using this Ga pseudopotential is also marked.

dopants V through Cu have multiple charge states that involve sequential filling of the localized states in the  $3d$  shell, resulting in magnetic ground states. The results shown here are PBE-LMCC results, using a 512-atom supercell, that comprehensively searches for all potentially stable charge states, and are from fully relaxed atomic configurations that include careful searches for Jahn-Teller distortions.

The  $d$ -electron state in a titanium dopant is relatively delocalized and weakly bound; the  $\text{Ti}_{\text{Ga}}$  proves to be a shallow donor. At the other end of the  $3d$  dopant series, the  $\text{Zn}_{\text{Ga}}$  is a shallow acceptor (comparable to an effective-mass ionization energy) [47]. Our calculations suggest it has a completely filled  $3d^{10}$  shell. In even the largest 1000-atom supercells our calculations cannot clearly distinguish the defect states and band states at the valence band edge, a result that agrees with the weak localization and negligible  $3d$  character found by Demchenko and Reshchikov [47].

The  $3d$  dopant defects all adopt high-spin  $d$ -state occupations in the ground state, except for the  $(1+)$  and  $(2+)$  charge states of the Co and the Ni defects where the  $e^\downarrow$  state becomes favored over the  $t_2^\uparrow$  state (filling the  $e$ -shell and reducing the overall spin state) and also the Fe $(2+)$  where the low-spin doublet  $e^\uparrow e^\downarrow$  displaces the high-spin quartet ( $e^\uparrow e^\uparrow t_2^\uparrow$ ) as the ground state (0.09 eV higher). Later (and deeper) in the  $3d$  dopant series, the crystal-field splitting dominates over the exchange stabilization, so that a (low-spin)  $e^\downarrow$  becomes occupied preferentially to a (high-spin)  $t_2^\uparrow$  state. Zakrzewski *et al.* [17] had obtained the same state-crossing behavior for the Co. We echo their suggestion that this represents an opportunity for discriminating experiments to test the validity of different theoretical approximations.

All these  $3d$  dopants have at least one deep acceptor state, that would act to compensate shallow donors, except the vanadium dopant  $\text{V}_{\text{Ga}}$ . It lacks a  $(1-)$  state, and would be ineffective in doping  $n$ -type GaN to obtain semi-insulating material. The Ni and Cu dopants additionally have a second acceptor state to form a  $(2-)$  defect. The  $3d$  dopants all also have deep donor states, making all of them (with the exception of the V above) amphoteric defects. Most have two donor states, to form a  $(2+)$ , like the Mn discussed above. The Cr and Fe exhibit additional stable  $(3+)$  states in these PBE-LMCC calculations, with  $(2+/3+)$  transitions near the VBE. The Fe $(3+)$ , however, is somewhat uncertain: the defect KS single-particle states are nearly merged with the VBE, and the  $(3+/2+)$  level position above the VBE is within the margin of accuracy of PBE-LMCC.

Illustrating the difficulties in obtaining unambiguous interpretation of experimental measurements, the position of the Fe $(1-/0)$  charge transition has been ascribed to measurements ranging from 2.5 eV by Baur *et al.* [48] to 3.17 eV by Heitz *et al.* [49]. A Fe $(1-/0)$  level at 2.86 eV is the most confident result, from the most recent measurements using optical absorption by Malguth *et al.* [50]. Our computed PBE value for  $(1-/0)$ , VB+2.78 eV in 1000-atom supercell, is well converged with supercell size, and agrees very well with this experiment. The computed  $(0/1+)$  charge transition at 0.72 eV agrees similarly well with the 0.75 and 0.73 eV obtained experimentally by Muret *et al.* [51]. Our calculations find yet additional transitions, at  $\sim 0.5$  eV for a  $(1+/2+)$  that is well converged and well resolved from the valence band,

and a  $(2+/3+)$  at  $<0.2$  eV that is not as well converged and not cleanly resolved from the VBE even in the 1000-atom supercell.

This agreement with experiment compares favorably against results obtained with hybrid functionals, which produced results ranging from 2.6 to 3.0 eV for the acceptor level [52–54]. Wickramaratne *et al.* additionally obtained a donor level at 0.26 eV above the VBE [54] but at a position 0.5 eV below the corresponding experimental measurement. The differences between the various reported hybrid functional results had been attributed to different empirical tuning of the exchange fraction in the hybrid functional [54], a tuning motivated by the desire to reproduce the experimental band gap within the single-particle energies. Our PBE results demonstrate that no such empiricism is necessary for computing defect levels in GaN. The full band gap emerges naturally from the total energy calculations using the LMCC boundary conditions, yielding roughly the same result for the acceptor level as (and a much better result for the donor level than) the hybrid functional calculations. An additional advantage is that finite-size errors in our local DFT calculations can be demonstrated to be fully eliminated in extension to large supercells, whereas the large computational expense of hybrid functionals largely limits routine calculations to much smaller supercells.

The Cu $(2+)$  defect is a special case that does not fit into the magnetic  $3d$  sequence. It is cleanly a localized state, judging from its KS single-particle state configuration, but has collapsed to a  $pD_{2d}$  singlet. Its existence was discovered from a comprehensive search for stable charge state configurations. The computed level at 0.2 eV below the VBE indicates this is a thermodynamically inaccessible state: the Cu $(2+)$  singlet is unreachable via a single-electron transition from the Cu $(1+)$  quartet ground state. The Cu $(1+)$  doublet excited state is reachable from this Cu $(2+)$  with a single-electron transition, with an associated defect level located within the band gap at VBE+0.06 eV. Given its anomalous status among  $3d$  dopants, and its thermodynamic instability, the Cu $(2+)$  was deemed an oddity not pertinent to this study, and not investigated further.

The collective defect level diagram vindicates the estimation of the defect band gap bounds derived from our earlier study of intrinsic defects in c-GaN [29]. The Fe $(2+/3+)$  level sits at  $\sim 0.1$  eV above the VBE, and the Ni $(2-/1-)$  is seen to be at  $\sim 3.3$  eV. This span closely matches the experimental band gap in c-GaN, indicating again that the PBE defect calculations are not hindered by a band-gap problem, provided that a proper control of charge boundary conditions via the LMCC (rather than jellium) is enforced.

The computed defect levels are rather well converged with respect to supercell size already at 216-atom supercells, usually to within 10 meV of the 512-atom supercell results. The 512-atom supercell results change from the 216-atom supercell results by more than 15 meV for only four near-edge levels: the near-VBE transitions for Fe, Ni, and Cu, and with the Ni $(2-/1-)$  near the CBE being the extreme case.

The good convergence of the computed Ni defect levels as a function of supercell size up to the  $5\times 5\times 5$  supercell with 1000 atoms is depicted in Fig. 8. The extreme case of Ni $(2-/1-)$  might not be fully converged even with the 1000-atom supercell, but the 512-atom results presented in

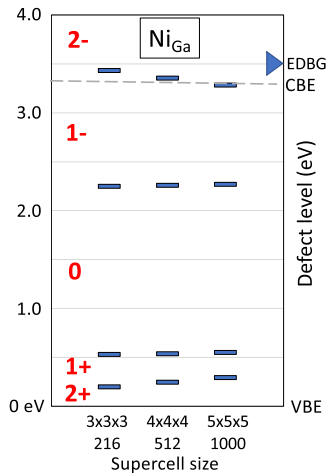


FIG. 8. Convergence of computed  $\text{Ni}_{\text{Ga}}$  defect levels with supercell size, from the small  $3 \times 3 \times 3$  supercells to the largest  $5 \times 5 \times 5$  supercells.

Fig. 7 can be deemed well converged, as documented in the detailed numerical data presented in Table S-1 of the Supplemental Material (SM) [55]. The density of state plots in Fig. 9 illustrate the distinction used to distinguish between localized states with Fermi levels that are cleanly within the band gap [Fig. 9(b) for the  $\text{Ni}(1-)$  defect] and lead to transition within the effective defect band gap (EDBG), and states that impinge upon a band edge that hybridize with a band-edge state [Fig. 9(a) for the  $\text{Ni}(2-)$  defect] and cannot be as cleanly resolved. Defect charge states that lead to Fermi levels outside the gap (the states lie outside the band edges) are rejected as candidates for localized transitions.

## 2. Jahn-Teller distortions

All of the JT-vulnerable defects, those defects that would exhibit a degenerate total ground state (metallic partially occupied states) in the symmetric  $T_d$  structure, are observed to undergo unmistakable symmetry-lowering distortions in these calculations. These distortions remove the degeneracy to create an electronically nondegenerate, insulating ground state. The optimal distortions are exclusively tetragonal distortions to structures with  $D_{2d}$  symmetry, with the sense of that distortion (pairing or resonant) being dictated by the  $t_2$  and  $e$  state occupations, independent of the chemical identity of the  $3d$  dopant. The ground-state structure for a given set of  $t_2$  and  $e$ -state occupations is depicted in Fig. 7. A singly occupied  $t_2$  spin shell ( $t_2^\uparrow$  or  $t_2^\downarrow t_2^\uparrow t_2^\uparrow$ ) leads to a paired- $D_{2d}$  structure, and doubly occupied  $t_2$  spin shell ( $t_2^\uparrow t_2^\uparrow$  or  $t_2^\downarrow t_2^\downarrow t_2^\uparrow t_2^\uparrow$ ), regardless of the occupancy within the  $e$  shell, leads to a resonant- $D_{2d}$  structure. A singly occupied  $e$ -spin-shell leads to a  $pD_{2d}$  structure, except in the case where a doubly occupied  $t_2$  shell dominates, such as in the  $d^5$  quartet- $(\uparrow \uparrow \circ \mid \uparrow \downarrow \uparrow)$  excited state for  $\text{Fe}(0)$  and  $\text{Co}(1+)$ . The  $e$  doubleton, being the deeper and more localized state than the  $t_2$ , has less influence on the bonds to the nitrogen neighbors.

Table S-3 in the SM [55] provides a detailed listing of the computed JT distortion energies, for each defect in its ground states and accessible spin excited states. As mentioned above,

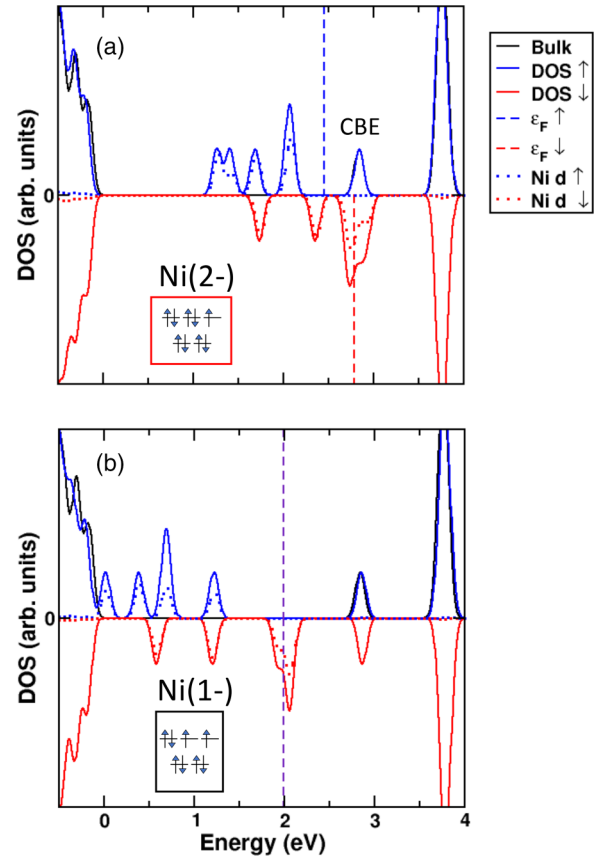


FIG. 9. Density of states for the (a)  $\text{Ni}(2-)$  and (b)  $\text{Ni}(1-)$  defects in the 216-atom supercell. Note that the highest KS state in the  $\text{Ni}(2-)$  impinges upon the CBE perfect supercell state. This causes a hybridization between the defect state and band edge that splits the  $t_2$  into an occupied doubleton and an empty singleton, that bracket the CBE state in the perfect crystal supercell (the clean CBE marker state is evident in the up-spin DOS). This state retains the large  $3d$  contribution (dotted lines) to the total state DOS, indicating a likely valid local defect state. This splitting and hybridization does not fully resolve in even the largest 1000-atom cell, as the defect state follows the CBE closely. The perfect crystal DOS is drawn in solid black, mostly overlaid by the defect DOS, the near perfect alignment of the crystal and defect bulk DOS testifying to the degree of localization of the defect states in the gap. The  $d^n$  occupation-distortion diagrams are taken from Fig. 7.

the  $e$ -shell-driven JT distortion energies are generally smaller than the  $t_2$ -driven distortions. The JT distortion energies range up to  $>0.2$  eV for the spin excited state for  $pD_{2d}\text{-Mn}(0)$  and  $rD_{2d}\text{-Fe}(0)$ , and also for the  $pD_{2d}\text{-Cu}(0)$  ground state. As the defect charge state approaches the band edge, the magnitude of a distortion decreases, most notably in the  $\text{Ni}_{\text{Ga}}(2+)$  ground state where the  $pD_{2d}$  distortion driven by the near CBE  $t_2$  is very weak. More often, however, the JT distortions for  $3d$  dopant charge states are significant and would need to be considered in any quantitative analyses of optical spectra involving these defects.

## 3. Vertical charge transition levels

The thermodynamic levels are indicative of, and are defined by, the stability of a given charge state as a function of

TABLE IV. The computed PBE-LMCC defect levels (thermodynamic) and vertical ionization potentials (VIP), and the second ionization levels (Level-2, VIP-2), for transition metal dopant atoms substituted on the Ga site in cubic GaN. The energies are in eV with respect to the inferred c-GaN valence band edge, within the 512-atom supercell model.

Element	V	Cr	Mn	Fe	Co	Ni	Cu
Transition-1	(0/1+)	(1-/0)	(1-/0)	(1-/0)	(1-/0)	(2-/1-)	(2-/1-)
Level-1	2.07	3.07	2.04	2.80	1.84	3.35	2.74
VIP-1	1.57	2.69	1.61	2.55	1.54	3.24	2.28
Transition-2	(1+/2+)	(0/1+)	(0/1+)	(0/1+)	(0/1+)	(1-/0)	(1-/0)
Level-2	1.39	2.44	1.46	0.71	0.88	2.26	1.40
VIP-2	0.93	1.91	0.87	0.52	0.49 <sup>a</sup>	1.96	1.14

<sup>a</sup>The thermodynamic (0/1+) level is between a spin quintet (0) and spin doublet (1+). The VIP is to a spin quartet (1+).

the Fermi level in the gap, and thus pertinent to the (technologically important) Fermi-level engineering to stabilize a desired defect charge state. Thermodynamic measurement of defect levels in wide-band-gap systems is challenging, in large part due to the greater depth of levels in the band gap. Optical measurements are generally less definitive [in one example mentioned above, Korotkov *et al.* [45] had ascribed their 1.42-eV observation to the  $\text{Mn}_{\text{Ga}}(1-/0)$ , later argued by Graf *et al.* [42] to be associated with an internal  $d \rightarrow d$  excitation], but are the more common experimental probes of charge transitions in wide-band-gap systems. The appropriate computation corresponding to such a measurement is a vertical ionization, where the atomic configuration does not change upon ionization. Table IV shows the computed vertical ionization potential (VIP) compared to the computed thermodynamic defect levels (depicted in Fig. 7).

The difference between the VIP and thermodynamic defect level is the structural relaxation energy of the ionized defect. In this table, it is seen that this relaxation amounts to  $\sim 0.3$ – $0.5$  eV across this entire set of defects and defect levels. With the exception of the  $\text{Co}(0/1+)$  transition, this does not affect the qualitative interpretation of the defect levels, but must be considered in any quantitative comparisons to optical measurements ascribed to charge transitions. In the  $\text{Co}(0/1+)$  ionization, the thermodynamic transition places the  $\text{Co}(1+)$  in its low-spin doublet ground state, but the vertical single-electron ionization instead takes the  $d^4$  quintet into a  $d^3$  high-spin quartet excited state, a qualitative distinction ensuing upon switching from an exchange-coupling dominated regime in the  $\text{Co}(0)$  to the crystal-field dominated regime in the  $\text{Co}(1+)$ .

#### 4. Spin-forbidden transitions

The energies of spin-forbidden luminescence involving  $e^\downarrow \rightarrow t_2^\uparrow$  transitions leading to change in defect spin state can be computed via differences between relaxed ground-state total energy DFT calculations of different spin, in a  $\Delta\text{SCF}$  (self-consistent field) approach described in Sec. III C. The special case of the  $d^2$  defects  $\text{V}(0)$ ,  $\text{Cr}(1+)$ ,  $\text{Mn}(2+)$ ,  $\text{Fe}(3+)$  is discussed later.

For the Mn and Fe dopants, we find stable quartet and doublet states in the calculations of  $d^3$  configurations, and quintet, triplet, and singlet states in the  $d^4$  configuration. The Fe and Co also have sextet, quartet, and doublet states in the  $d^5$  and a quintet ground state and a triplet excited state in

the  $d^6$ . The computed relative energies of all these stable spin states for each defect are provided in Table S-3 in the SM. The calculated excitation energies from the predicted ground-state spin state to the adjacent spin state (i.e., accessible by a single spin flip) are presented in Table V.

In addition to the full  $\Delta\text{SCF}$ , which would correspond to a DFT prediction of the zero-phonon line (ZPL) energy, Table V quotes the Koopmans-inspired estimates using the DFT single-particle eigenenergies in both the ground-state structure and in the excited-state structure. The quality of these estimates can be assessed in comparison to the full  $\Delta\text{SCF}$ , an assessment useful for the later analysis of spin-conserving excitations. For  $\text{Fe}(0)$  and  $\text{Mn}(0)$  we performed SCF calculations corresponding to these single-particle excitations (without a structural relaxation) to resolve the contributions to the difference between the single-particle and  $\Delta\text{SCF}$  predictions. The single-particle  $\Delta\epsilon$  typically overstate the  $\Delta\text{SCF}$  excitation energy by 0.3–0.7 eV. This difference is mostly from an electronic relaxation in the SCF with a lesser contribution from the structural relaxation (comparable to a JT distortion energy). A cautionary aspect is that many of the excited states, e.g., the  $\text{Fe}(2+)$ , have single-particle level structures that deceptively might suggest these were a ground state (those with a negative  $\Delta\epsilon$  in Table V).

As mentioned above, the observed 1.25-eV luminescence in Mn-doped w-GaN had originally been (tentatively) attributed to the sextet-quartet  $e^\downarrow \rightarrow t_2^\uparrow$  excitation in  $\text{Mn}(1-)$  [43], but was proposed to be more likely attributed to the quintet-triplet excitation in  $\text{Mn}(0)$  [17]. Our calculated  $\Delta\text{SCF}$  of this quintet-triplet excitation of 1.0 eV is an underestimate of this excitation energy. This result is also lower but similar to the value quoted by Zakrzewski *et al.* [17] using the same PBE functional.

Hybrid functional calculations in literature [14] make no mention of this intracenter process in  $\text{Mn}(0)$ . With the occupied  $d^\uparrow$  states obtained with hybrid HSE functional buried several eV below the VBE there is no possibility of a  $t_2^\uparrow \rightarrow e^\downarrow$  transition to create the triplet state. The PBE calculations succeed in predicting the existence of this observed excitation for which the ostensibly better hybrid functionals fail.

The calculations further indicate that the  $\text{Mn}(1+)$  should also exhibit a spin-forbidden transition. Our results show a doublet excited state  $\sim 0.3$  eV above the high-spin quartet ground state. The  $\text{Mn}(1+)$  is stable within a small range of Fermi level that potentially could be engineered in heavily Mg

TABLE V. Computed excitation energies, from the ground-state spin state to the excited spin state. The  $\Delta\text{SCF}$  is the DFT energy difference between the fully relaxed structures (see Sec. III C). The  $\Delta\epsilon$  is the difference in the Kohn-Sham eigenvalues corresponding to the spin flip in the ground-state and excited-state structure, as described by the spin configuration ( $t_2^x t_2^y t_2^z | e^u e^v$ ), an estimate for the excitation energy in a Koopmans-type interpretation of the single-particle states. The  $\Delta\epsilon_{\text{GS(ES)}}$  listed for Mn(0) and Fe(0) are the computed “vertical” energies of excitations in the relaxed GS (ES) structure, i.e., the self-consistent evaluation of the spin-flipped energy represented by the  $\Delta\epsilon$ .

	Mn(1+) $d^3$	Fe(2+) $d^3$	Fe(0) $d^5$	Co(1+) $d^5$
GS	( $\uparrow \circ \circ   \uparrow \uparrow$ )	( $\circ \circ \circ   \uparrow \downarrow \uparrow$ )	( $\uparrow \uparrow \uparrow   \uparrow \uparrow$ )	( $\uparrow \circ \circ   \uparrow \downarrow \uparrow \downarrow$ )
$\Delta\epsilon_{\text{GS}}$	0.99	0.63	1.33	0.54
$\Delta_{\text{GS}}$			1.14	
$\Delta\text{SCF}$	0.33	0.09	0.92	0.20
$\Delta_{\text{ES}}$			0.87	
$\Delta\epsilon_{\text{ES}}$	-0.33	-0.45	0.40	-0.11
ES	( $\circ \circ \circ   \uparrow \downarrow \uparrow$ )	( $\uparrow \circ \circ   \uparrow \uparrow$ )	( $\uparrow \uparrow \circ   \uparrow \downarrow \uparrow$ )	( $\uparrow \uparrow \circ   \uparrow \downarrow \uparrow$ )
	Mn(0) $d^4$	Fe(1+) $d^4$	Fe(1-) $d^6$	Co(0) $d^6$
GS	( $\uparrow \uparrow \circ   \uparrow \uparrow$ )	( $\uparrow \uparrow \circ   \uparrow \uparrow$ )	( $\uparrow \uparrow \uparrow   \uparrow \downarrow \uparrow$ )	( $\uparrow \uparrow \uparrow   \uparrow \downarrow \uparrow$ )
$\Delta\epsilon_{\text{GS}}$	1.74 <sup>a</sup>	0.82	1.80	0.46
$\Delta_{\text{GS}}$	1.19			
$\Delta\text{SCF}$	0.99	0.40	1.13	0.21
$\Delta_{\text{ES}}$	0.87			
$\Delta\epsilon_{\text{ES}}$	0.20	-0.13	0.40	-0.04
ES	( $\uparrow \circ \circ   \uparrow \downarrow \uparrow$ )	( $\uparrow \circ \circ   \uparrow \downarrow \uparrow$ )	( $\uparrow \uparrow \circ   \uparrow \downarrow \uparrow \downarrow$ )	( $\uparrow \uparrow \circ   \uparrow \downarrow \uparrow \downarrow$ )

<sup>a</sup>Note: the empty  $e^\downarrow$  state KS eigenvalue is  $\sim 0.1$  eV above the CBE KS eigenvalue in the quintet ground state, but is brought 0.4 eV below the CBE when occupied in the vertical excitation calculation.

co-doped GaN. The Fe exhibits multiple spin states in each of its (2+) through (1-) charge states.

A sharp luminescent line observed in GaN:Fe at 1.30 eV [56] has been attributed to the  ${}^4T_1 \rightarrow {}^6A_1$  internal transition at the  $\text{Fe}_{\text{Ga}}(0)$ . Zakrzewski *et al.* [17] had quoted a quartet excitation energy using GGA (PBE) that matched this observation. Our full  $\Delta\text{SCF}$  (self-consistent field) PBE for the sextet-quartet excitation energy is only 0.92 eV (with a second, doublet-spin excited state another 0.46 eV above the quartet-spin excited state). Figure 10 depicts the single-particle density of states obtained from these self-consistent calculations. The triplet of  $t_2^\uparrow$  single-particle states lies  $\sim 0.4$  eV above the VBE when fully occupied in the sextet  $T_d$  ground state. The vacated single-particle state splits off and shifts almost 0.9 eV higher in the quartet  $tD_{2d}$  excited state. The empty  $e$  single-particle states that sit 1.1 eV below the CBE in the sextet ground state are split in the JT-distorted quartet, with the newly occupied state slightly lowered by 0.1 eV after the excitation.

Our PBE  $\Delta\text{SCF}$  result for this excitation energy differs from the earlier PBE report. Zakrzewski *et al.* [17] had not specified how they had obtained their quoted value. It is likely, however, that they quoted a  $\Delta\epsilon$ : a difference in Kohn-Sham eigenvalues. As shown in Table V [and illustrated in the DOS of Fig. 10(a)], we obtain 1.33 eV for  $\Delta\epsilon_{\text{GS}}$  between the occupied  $t_2^\uparrow$  and empty  $e^\downarrow$  single-particle levels. This agrees with the quoted Zakrzewski value. Supporting this inference, they also quoted a 2.1-eV energy for a  $t_2^\uparrow \rightarrow t_2^\downarrow$  transition in Fe(0), which matches the 2.0 eV we find for the corresponding  $\Delta\epsilon_{\text{GS}}$  (this  $\Delta\text{SCF}$  is not accessible via ground-state DFT, this being an excited state within the quartet).

Our PBE results thus agree with and confirm the Zakrzewski results. Although the Koopmans-inspired  $t_2^\uparrow \rightarrow e^\downarrow$  transition agrees with the experimental PL datum [56], the more appropriate  $\Delta\text{SCF}$  comparison significantly underestimates the 1.30-eV PL significantly, by 0.4 eV. This deviance is larger than the (0.1–0.2)-eV accuracy typically observed in PBE-LMCC defect levels derived from total energy calculations (an accuracy further supported in the current calculations of the acceptor levels for Mn and Fe).

One possible conclusion is that the DFT in GaN incurs larger errors than the (0.1–0.2)-eV accuracy seen elsewhere. Another possibility is that this PL transition is incorrectly assigned. A more viable candidate for this observed PL is the  $t_2^\uparrow \rightarrow t_2^\downarrow$  transition. The  $\Delta\epsilon_{\text{GS}}=2.0$  eV for this transition, but as seen in other transitions presented in Table V, the more physically correct  $\Delta\text{SCF}$  (corresponding to a zero-phonon line, ZPL) often leads to values  $\sim 0.7$  eV lower than the corresponding  $\Delta\epsilon_{\text{GS}}$ . A relaxation of this magnitude from the  $\Delta\epsilon_{\text{GS}}$  for this transition would be consistent with the observed PL line. Absent further systematic studies coordinating experiment and theory to disambiguate the source of PL, and ensure that theory and experiment are indeed measuring the same process, it is not possible to conclusively determine whether this result indicates a degraded accuracy of DFT in GaN, or whether this mandates reassessing the (often speculative) assignments made in PL experiments.

Hybrid functionals, through an empirical tuning of the exchange fraction to reproduce the band gap within the single-particle Kohn-Sham levels, are commonly claimed to improve upon the accuracy of local DFT. Wickramaratne *et al.* [54] had recently investigated the  $\text{Fe}_{\text{Ga}}$  and quoted a  $\Delta\text{SCF}$  result for the sextet-quartet excitation of 1.55 eV for Fe(0), which

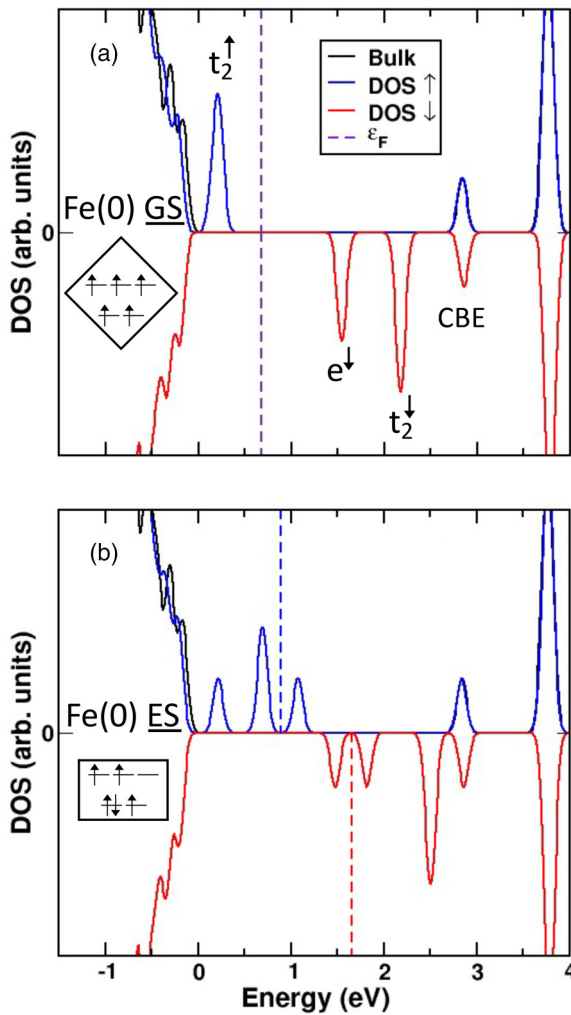


FIG. 10. Computed PBE density of states (DOS) in  $\text{Fe}_{\text{Ga}}(0)$  for (a) the sextet ground state  $\underline{\text{GS}}$ ; and (b) the quartet excited state  $\underline{\text{ES}}$  obtained from the relaxed self-consistent calculation after a  $t_2^\uparrow \rightarrow e^\downarrow$  transition. Note that all the involved single-particle states are in the KS band gap in both the  $\underline{\text{GS}}$  and  $\underline{\text{ES}}$ , indicating a local  $d \rightarrow d$  transition. The perfect crystal DOS is drawn in solid black, mostly overlaid by the defect DOS, the near perfect alignment of the crystal and defect bulk DOS testifying to the degree of localization of the defect states in the gap.

overshoots the PL observation by 0.25 eV. However, their DOS for the sextet ground state depicts no occupied  $d$  single-particle states within the band gap to accommodate the imputed internal  $t_2^\uparrow \rightarrow e^\downarrow$  transition. The empty  $e^\downarrow$  just above the CBE might be viable as the target of the transition, but the occupied  $t_2^\uparrow$  single-particle states are buried in a broad resonance 5–8 eV below the VBE. It is implausible that such deeply buried states would lead to a localized sharp internal PL transition, and invites the question whether a stable local quartet spin state for the  $\text{Fe}_{\text{Ga}}$  exists with hybrid functionals. As pointed out by Zakzrewski *et al.* [17], hybrid functional results for Mn and Fe lead to deeply buried occupied  $d$  states, that preclude intrasite  $d \rightarrow d$  transitions that might lead to photoluminescence.

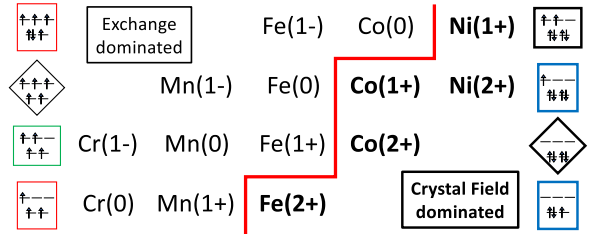


FIG. 11. Boundary between exchange-coupling-dominated and crystal-field-dominated regimes for 3d dopant ground states. This boundary is only meaningful for the  $d^3$  through  $d^6$  defects shown. The  $d^7$  defects all have completely full  $e$  shells in their high-spin ground states, and the  $d^2$  defects have a high-spin ground state occupying only the  $e$ -shell orbitals. Color-shape coding for the  $d^n$  occupation-distortion diagrams is taken from Fig. 7.

Experiments had previously ascribed observed PL to these spin-forbidden transitions in neutral Mn and Fe defects. The results presented in Table V indicate the DFT energies of additional spin-forbidden transitions accessible from the lowest-energy spin state. All of the (high-spin) Fe charge states possess spin excited states stemming from a  $t_2^\uparrow \rightarrow e^\downarrow$  excitation. In addition to these previously known Mn and Fe spin-forbidden transitions, the Co dopant also is predicted to have (low-energy) transitions in its (0) and (1+) charge states. It is notable that the  $d^5$  Co(1+) has the same quartet excited state as its isoelectronic Fe(0) neighbor, but the high-spin Fe sextet ground state is replaced by a low-spin doublet ground state in Co. The experimental confirmation, or refutation, of the existence (and location) of these Co spin-forbidden transitions would be a sensitive test of the theory and the boundary between exchange- and crystal-field-dominated regimes. Figure 11 shows the boundary between the regimes where exchange-coupling dominates the ground state and the crystal field dominates the ground state. This predicted boundary will be functional specific and represent a sensitive measure of the accuracy of a theory.

The Cr, except for the (1+) charge state discussed below, is seen to have no spin-forbidden excited states in these calculations. The necessary unoccupied single-particle states in all  $\text{Cr}_{\text{Ga}}$  charge states are inaccessible because they disappear above the CBE. The Ni dopant also has no spin-flip excited states, the necessary occupied  $d$  states disappear below the VBE.

The results in Table V indicate that single-particle energies from the PBE results are (surprisingly) qualitatively and semiquantitatively predictive of excitation energies. Nonetheless, using single-particle energies for quantitative predictions should be done cautiously. The necessary corrections are observed to take two aspects: an electronic relaxation involving an SCF calculation corresponding to the appropriate occupations of single-particle states, and a structural relaxation. The larger part of this correction to the Koopmans-type single-particle estimate to the full  $\Delta\text{SCF}$  transition energies comes from the electronic relaxation in the SCF in the calculation of the vertical excitation energy  $\Delta_{\text{GS(ES)}}$ . Moreover, we observe that the single-particle energies can be misleading; as often as not, the single-particle energies in the excited spin state structure would indicate it to be the ground state: the (empty)

TABLE VI. Energies for  $S = 0$  and  $S = 1$  excited states for  $d^2$  transition metal dopants (in eV) from the triplet  $e^\uparrow e^\uparrow$  GS.

	V(0)	Cr(1+)	Mn(2+)	Fe(3+)
Experiment	0.93 [57]	1.19 [57]	1.04 [58] <sup>a</sup>	
$S = 0$ $\Delta$ SCF	1.09	1.11	0.87	$\sim 0.3$ <sup>b</sup>
$S = 0$ $\Delta\epsilon_{\text{GS}}$	$\epsilon(e^\downarrow) \gg \text{CBE}$	2.19	(1.4) <sup>c</sup>	$\epsilon(e^\uparrow) \ll \text{VBE}$
$S = 1$ $\Delta\epsilon_{\text{GS}}$	(1.2) <sup>c</sup>	1.69	(1.4) <sup>d</sup>	$\epsilon(e^\uparrow) \ll \text{VBE}$

<sup>a</sup>Excitation of a  $d^2$  state (Mn<sup>5+</sup> oxidation state) ascribed to a Mg-Mn-Mg complex.

<sup>b</sup>The Fe(3+)  $S = 0$  excited state is not cleanly resolved from the VBE.

<sup>c</sup>The occupied  $e^\uparrow$  single-particle eigenstate is below the VBE state, by  $\sim 0.3$  eV.

<sup>d</sup>The empty  $t_2^\uparrow$  triplet eigenstate is above the CBE, but can be cleanly resolved at CBE+0.60 eV.

single-particle eigenstate corresponding to the ground-state occupancy is *above* the (occupied) single-particle state into which that electron has been promoted. The structural relaxation, e.g., changes in Jahn-Teller distortions, prove to be slightly smaller. These contributions combine to give full  $\Delta$ SCF transition energies that are to be 0.2–0.8 eV relaxed from the  $\Delta\epsilon$ , regardless of whether started from exciting from the ground-state structure or from deexciting from the excited-state structure.

### 5. The $d^2$ dopants

The defect states with  $d^2$  electronic configurations, the V(0), Cr(1+), Mn(2+), and Fe(3+), all take a high-spin triplet as their electronic ground state. This is the expected configuration within the standard model, the Hund's rule dictating a high-spin coupling of the electrons within the  $e$  doublet:  $e^\uparrow e^\uparrow$ . This nondegenerate electronic ground state predicts the triplet  $d^2$  configuration retains the full  $T_d$  symmetry, as depicted in Fig. 7.

Within an exchange-dominated regime, the expected lowest *excited state*, via promoting an electron in a  $e^\uparrow \rightarrow t_2^\uparrow$  transition, is the triplet state:  $e^\uparrow t_2^\uparrow$ . Reflecting this expectation, the PL peak at 1.19 eV observed for Cr(1+) was first associated with emission from this triplet [45]. However, this PL was later assigned instead to emission from an open-shell singlet related to the ground state by a  $e^\uparrow \rightarrow e^\downarrow$  spin flip:  $e^\uparrow e^\downarrow$ .

Table VI presents the analysis for the excited-state energies in the  $d^2$  defects, for the triplet ( $S = 1$ ) and singlet ( $S = 0$ ). Each  $d^2$  dopant yields a  $S = 0$  excited state, with the Fe(3+) being only marginally stable in these calculations (the  $e$  doublet single-particle states lie right at the VBE state). The computed  $\Delta$ SCF for the Cr(1+)  $S = 0$  excited-state energy, 1.11 eV above the ground state, agrees extraordinarily well with the measure PL for this transition, 1.19 eV [57], providing additional evidence for the assignment of this PL to the singlet excitation as opposed to the triplet excitation.

The  $S = 0$   $\Delta$ SCF for the V(0), 1.09 eV, would represent similarly good agreement with the V(0) PL peak at 0.93 eV [57], but it is not evident that this would be the correct assignment. Examining the single-particle KS energies in the ground

state, the empty  $e^\downarrow$  eigenstate, the destination of the spin-flip transition, disappears above the CBE. The computed existence of the  $S = 0$  in the calculations demonstrates that this state can be drawn out of deep in the CB. This observation is anecdotal caution about placing great confidence in Koopmans-type interpretations of single-particle energies. The empty  $t_2^\uparrow$  state needed to create the triplet excited state also lies above the CBE, but the triplet KS eigenstates can be unambiguously distinguished from the CB states at 0.60 eV above the CBE. The  $\Delta\epsilon$  estimate of the triplet excitation is 1.2 eV. The observation of the PL demonstrates the existence of a stable excited state, so for the theory to describe this, either the  $t_2^\uparrow$  or the  $e^\downarrow$  in the DFT must be drawn into the band gap. While a  $\Delta$ SCF of this excitation is not possible in standard DFT, the expected electronic and structural relaxations are almost certainly large enough to make this triplet state more stable than the singlet excited state, in a reversal of the order discovered for the Cr(1+). Experiments to resolve the spin of the V(0) excited state would be very useful in assessing the validity of the DFT analysis.

For the Mn(2+), the complication in the analysis arises instead for the occupied  $e^\uparrow$  state. The occupied  $e$  doublet has sunk below the VBE, by roughly 0.3 eV. Once more, that the  $S = 0$  excited state exists in the calculation demonstrates that a KS eigenstate can be drawn into the KS band gap. The  $t_2^\uparrow$  and the  $e^\downarrow$  states are nearly degenerate, leading to a  $\Delta\epsilon = 1.4$  eV. The  $\Delta$ SCF for the singlet predicts an excitation energy of 0.87 eV. With the (1+/2+) transition for Mn being 1 eV above the VBE, it might be possible to observe this defect center in appropriately doped  $p$ -type GaN. Devillers *et al.* [58] observed a transition at 1.04 eV in  $p$ -type Mg-doped GaN, that they determined to be an intrasite emission in Mn( $d^2$ ), a  $d$  configuration on the Mn they hypothesized was stabilized as part of a Mg-Mn-Mg complex.

The Fe(3+) is only barely stable. It exists in a small range of Fermi level very close to the VBE, if it exists at all. The occupied  $e^\uparrow$  state has sunk far below the VBE, making viable local excitations out of this state highly implausible. A singlet excited-state calculation is almost stable, with the singlet  $e$  doublet right at the VBE. Lying so close to the VBE, this Fe(3+) defect center almost certainly cannot be stabilized through chemical doping.

The Cr(1+) is distinctive in this set: all the requisite single-particle states, the occupied  $e^\uparrow$  and unoccupied  $e^\downarrow$ , and  $t_2^\uparrow$  lie in the KS band gap. Nonetheless, an excited-state PL in V(0) demonstrates that this existence criterion is not strictly followed. However, the DFT analysis indicates this excited state will be a less useful (short-lifetime) triplet excited state rather than the longer-lifetime singlet seen in Cr(1+). The Mn(2+) likely has the same electronic characteristics as Cr(1+).

In summary, while the ground states of the  $d^2$  defect centers are ruled by an exchange-stabilized regime, the electronic configuration of the excited states is dominated by crystal-field splitting, the  $e^\uparrow e^\downarrow$  preferred over the  $e^\uparrow t_2^\uparrow$  triplet, except perhaps for the earliest V(0) case.

### 6. Spin-conserving transitions

Excited states corresponding to  $e^\uparrow \rightarrow t_2^\uparrow$  (or  $e^\downarrow \rightarrow t_2^\downarrow$ ) spin-conserving single-particle promotions are not directly

TABLE VII. Spin-conserving  $e \rightarrow t_2$  transitions, as computed from a single particle  $\Delta\epsilon$  in the ground-state structure within the PBE approximation.

Defect	Transition	$\Delta\epsilon$	Experiment
V(0)	$e^\uparrow \rightarrow t_2^\uparrow$	1.19	0.93 <sup>a</sup>
V(1+)	$e^\uparrow \rightarrow t_2^\uparrow$	1.28	
Cr(1-)	$e^\uparrow \rightarrow t_2^\uparrow$	0.93	
Cr(0)	$e^\uparrow \rightarrow t_2^\uparrow$	1.27	
Cr(1+)	$e^\uparrow \rightarrow t_2^\uparrow$	1.69	1.19 <sup>a</sup>
Mn(0)	$e^\uparrow \rightarrow t_2^\uparrow$	1.37	1.42 <sup>b</sup>
Mn(1+)		$e^\uparrow < \text{VBE}$	
Mn(2+)		$e^\uparrow < \text{VBE}$	
Mn( <i>p</i> -type)			1.0 <sup>c</sup> “Mn(1+)” 1.04 <sup>d</sup> “Mg-Mn( $d^2$ )-Mg” 0.39 <sup>e</sup>
Fe(1-)	$e^\downarrow \rightarrow t_2^\downarrow$	0.61	
Fe(1+)	<u>GS</u> ( $S = 2$ ) <u>ES</u> ( $S = 1$ ) <u>ES</u> ( $S = 1$ )	$e^\uparrow \rightarrow t_2^\uparrow$ $e^\downarrow \rightarrow t_2^\downarrow$ $e^\downarrow \rightarrow t_2^\downarrow$	$e^\uparrow < \text{VBE}$ 0.94 1.04
Fe(2+)		$e^\downarrow \rightarrow t_2^\downarrow$	0.95
Co(0)	<u>GS</u> ( $S = 2$ ) <u>ES</u> ( $S = 1$ )	$e^\downarrow \rightarrow t_2^\downarrow$ $e^\uparrow \rightarrow t_2^\uparrow$	1.06 0.71
Co(1+)	<u>GS</u> ( $S = \frac{1}{2}$ ) <u>ES</u> ( $S = \frac{3}{2}$ ) <u>ES</u> ( $S = \frac{5}{2}$ )	$e^\downarrow \rightarrow t_2^\downarrow$ $e^\uparrow \rightarrow t_2^\uparrow$ $e^\uparrow < \text{VBE}$	1.02 1.17 $e^\uparrow < \text{VBE}$
Ni(1-)	$e^\downarrow \rightarrow t_2^\downarrow$	1.46	
Ni(0)	$e^\downarrow \rightarrow t_2^\downarrow$	1.35	1.05 <sup>f</sup>
Cu(1-)	$e^\downarrow \rightarrow t_2^\downarrow$	1.55	

<sup>a</sup>From Baur *et al.* (1995) [57].<sup>b</sup>From Korotkov *et al.* (2002), ascribed to the (1- / 0) charge transition [45]; reassigned to an internal excitation by Graf *et al.* [42].<sup>c</sup>From Han *et al.* (2004) [59].<sup>d</sup>From Devillers *et al.* (2012) [58] and assigned to a Mn( $d^2$ ) electronic configuration.<sup>e</sup>From Malguth *et al.* (2006) [50].<sup>f</sup>From Pressel *et al.* (1996) [60].

accessible using standard DFT because the DFT is only strictly valid for the ground-state single-particle occupations. Table VII shows the  $\Delta\epsilon$  for the lowest-energy spin-conserving  $e \rightarrow t_2$  transitions accessible within the PBE approximation for each of the 3d dopant atoms. Those charge states not listed in the table do not have an accessible single-particle transition: either the necessary occupied  $e$  single-particle state is below the VBE or the target empty  $t_2$  single particle is above the CBE. Three such examples are listed in Table VII: in the high-spin sextet excited state (0.12 eV above the low-spin ground state) of Co(1+), in the high-spin quintet ground state (only 0.10 eV more stable than the low-spin singlet) of Fe(1+), and for the Mn(1+) ground-state quartet. In these cases, the occupied  $e$  single-particle states are driven well below the VBE and are not accessible for an intrasite transition.

The computed single-particle  $\Delta\epsilon=1.19$  eV for V(0) is a good predictor of the experimental PL transition at 0.93 eV ascribed to the V(0) [57], especially considering the expected electronic and structural relaxation from the  $\Delta\epsilon$  to the full  $\Delta\text{SCF}$  observed in the spin-flip calculations in Table V. Our results for V(0) and V(1+) agree well with the values obtained by Gerstmann *et al.* [6] (1.12 and 1.33 eV, respectively), surprisingly well considering that these earlier results used a different functional (LDA) in a much smaller computational

model that included no lattice relaxations. This agreement must be deemed mostly accidental.

Our calculations predict accessible  $e^\uparrow \rightarrow t_2^\uparrow$  intrasite transitions for Cr(1-), Cr(0), and Cr(1+). Baur *et al.* had ascribed the measured zero-phonon line at 1.193 eV to Cr(1+), which is consistent with the computed  $\Delta\epsilon=1.69$  eV (when reduced by an electronic and structural relaxation). The Cr(0) and Cr(1-) exhibit significantly smaller  $\Delta\epsilon$  transition energies than the Cr(1+). This can be rationalized as the extra Coulombic repulsion from additional  $d$  electrons leading to more delocalized states.

Zakrzewski *et al.* had previously quoted a computed result for Mn(0) at  $\sim 1.4$  eV [17], and our result agrees with theirs. This is the only viable  $e^\uparrow \rightarrow t_2^\uparrow$  single-particle transition from the ground state for any Mn charge state. Han *et al.* [59] had reported PL peaks at  $\sim 1.0$  eV that appeared in heavily Mg-doped (*p*-type) GaN, which they ascribed to an intrasite excitation at Mn(1+). The single-particle states in the PBE calculation in the quartet Mn(1+) ground state disagree: we do not predict this transition. The occupied  $e^\uparrow$  single-particle states have merged into the bands below the VBE. It is possible that a self-consistent calculation of the transition would draw the requisite  $e^\uparrow$  above the VBE, accommodating a transfer of the electron to the  $t_2^\uparrow$  state, but this

is not evident in the single-particle spectrum of the ground state.

Hybrid functional calculations in Mn [14] and Fe [54] had not reported spin-conserving excitations. The needed  $e$  single-particle states in these hybrid functional calculations are buried deeply under the VBE, even for the Mn(0) and Fe(1−) for which the intrasite excitations are experimentally well established. Our results for Mn(1+) show that the PBE also might be (erroneously) prone to placing the occupied  $e$  too deep. The  $d$  states in the Mn(0) lie right at the VBE using PBE, making a local  $e^\uparrow \rightarrow t_2^\uparrow$  transition possible, but are drawn below the VBE with the Mn(1+), leaving no candidate for the observed 1.0-eV excitation Han *et al.* [59] attributed to the Mn(1+). Devillers *et al.* similarly observed a PL at 1.04 eV in heavily Mg-codoped GaN assigned to  $S = 0$  excited state, that they attributed to a Mn complexed to two Mg acceptors, an alternate model for this observation.

Our predicted single-particle transition with  $\Delta\epsilon = 0.61$  eV for Fe(1−) compares favorably with the observed PL at 0.39 eV [50]. No spin-conserving transitions are possible in Fe(0) with its high-spin  $d^5$  ground state. The ground state in the Fe(1+) is predicted to be a high-spin quintet. The PBE result has no spin-conserving single-particle transitions, as the occupied  $e^\uparrow$  sink below the VBE. However, the low-spin singlet state is computed to be only 0.10 eV higher than the quintet ground state (the intervening triplet is 0.40 eV higher), and is seen to have a  $e^\uparrow \rightarrow t_2^\uparrow$  transition at 0.94 eV and a  $e^\downarrow \rightarrow t_2^\downarrow$  transition at 1.04 eV. The Fe(2+) similarly has a close competition between a quartet and doublet configuration, the low-spin state being lower than the quartet by 0.09 eV. Once again, the low-spin state possesses a  $e^\uparrow \rightarrow t_2^\uparrow$  single-particle transition in the gap, at 0.95 eV, while the high-spin state buries the  $e^\uparrow$  below the VBE. This distinction between the PL accessible in the high-spin (none) and low-spin (near 1 eV) could serve as a discriminating experimental test of the boundary between regimes dominated by exchange coupling and crystal-field splitting, and also serve as a discriminating test of the fidelity of different DFT approximations.

The cobalt results also reveal a close competition between different spin states in its (1+) charge state, the singlet, triplet, and quintet states have formation energies within 0.2 eV of each other. Once again, the high-spin calculation predicts an absence of spin-conserving transitions, while the other spin states have single-particle transitions at  $\gtrsim 1$  eV. This also could serve as a good test case to assess the balance between exchange coupling and crystal-field splitting. The high- and low-spin Co(0) can not be discriminated this way. Both the high- and low-spin states are computed to have accessible single-particle transitions, but the DFT is not accurate enough to discriminate between these on the basis of the computed energies. Two of the Ni and Cu charge states are predicted to be capable of  $e^\downarrow \rightarrow t_2^\downarrow$  transitions. The Ni(0) with a  $\Delta\epsilon = 1.35$  provides good agreement with the PL peak at 1.05 eV ascribed to the  $d^7$  state in Ni [60].

Despite the admonition that the eigenstates and eigenvalues of the DFT Kohn-Sham equations must not be interpreted as corresponding to elementary excitations [35], the single-particle  $\Delta\epsilon$  approach is seen in Table VII to yield useful, semiquantitative estimates to the excitation energy. These es-

timates can be remarkably accurate if one invokes corrections for the missing electronic and structural relaxation effects. From the spin-forbidden (spin-flip) transition results in Table V where  $\Delta\text{SCF}$  are possible using ground-state DFT, these relaxation effects amount to 0.2–0.7 eV. That relaxation energy closely matches the 0.2–0.5 eV overstatement seen in the  $\Delta\epsilon$  with respect to the experimental PL energies for the spin-conserving transitions here. The exception is the Mn(0) transition, where the  $\Delta\epsilon = 1.37$  eV closely matches the experimental value of 1.42 eV. This PL assignment to the Mn(0) should be more carefully and skeptically examined. Additional self-consistent relaxations from the  $\Delta\epsilon$  estimate will significantly reduce this predicted value and its apparent, and misleading, agreement with experiment, calling into question the association of this particular excitation with the experiment PL peak. The computed excitation would be more numerically consistent with the 1.0-eV PL Han *et al.* had associated with the Mn(1+) [46]. With this exception, the close correspondence of the calculated PBE values with the known experimental values augurs well for the PBE predicted transitions in those cases where experiments are not yet available.

## V. DISCUSSION

We begin with a discussion concerning the relation of this work to a debate concerning the hybridization of the  $3d$  orbitals for the  $M_{\text{Ga}}$  dopants with neighboring nitrogen  $p$  orbitals. That the Mn(0) might be better described as a  $d^5 + h^+$  [the hole localized predominantly on the N( $p$ ) neighbors] rather than a  $d^4$  (with the defect state strongly localized on the  $3d$  orbitals of the Mn dopant) was first proposed by Dietl and coworkers [61]. This debate has prompted several experimental works [1,62,63] and associated theory efforts [64–66] to probe this distinction. From the perspective of the DFT calculations, this is a distinction without meaningful difference. The computed defect states will always hybridize between the dopant  $3d$  orbitals and the N orbitals of the valence band through a variational process [66–68]. The theory analysis of Nelson *et al.* showed “the feasibility of both the effective  $d^4$  and  $d^5$  descriptions” and concluded that the  $d^4$  is the simplest means to describe local properties of isolated Mn atoms (the focus of our study) and that the  $d^5$  is most suitable for long-range interactions determining long-range magnetic order between Mn atoms. The analysis of Stefanowicz *et al.* [62] concluded that the experimental record collectively “cannot tell the difference between  $d^4$  and  $d^5$  models of the Mn<sup>+3</sup> state” for the Mn(0). Experiments cannot meaningfully distinguish between these artificial limits and theory dictates that these states will always be hybridized on a continuous spectrum between these limits. Our DFT results for isolated  $3d$  dopants (defect levels, distortions) are conceptually well described by the local- $3d$  conceptual framework described in Sec. II, and are fully consistent with Nelson’s conclusion concerning the validity of this standard model for local properties of isolated  $3d$  defects. We observe this hybridization in the DOS plots for Ni presented in Fig. 9, where the gap defect states are associated with strong  $3d$  character that clearly include hybridization with N neighbors, yet the Ni defect levels are nonetheless categorized cleanly with a crystal-field-split  $3d$  model. The DFT results in this paper for

isolated 3d dopants are most concisely and usefully framed within a conceptual model depicting the defect occupations as localized 3d states.

The computed defect level structure in Fig. 7 expresses a regularity that reveals the strong role that exchange stabilization plays in the description of the local 3d dopants. The closed spin-shell defect centers (empty, full, or high-spin half-filled manifolds), with a total nondegenerate electronic ground state which therefore retain a symmetric  $T_d$  structure, are stable over a larger range of Fermi level than the JT-distorted charge states. More than a theoretical curiosity, this has technological implications because of the ease with which a given defect center can be created. For example, the Cr(1+) center showing such great promise as a quantum center [2], is stable over a span of almost 2 eV, whereas the other charge states with partially occupied (and JT-distorted) shells have much narrower ranges of Fermi level where they are stable. The discovery of the Cr(1+) center was likely facilitated by its wide range of stability: either Mn doping of  $n$ -type GaN pins the Fermi level at the Mn(1−/0) transition at 2.0 eV or doping of  $p$ -type GaN to pins the Fermi level at the Mn(1+/2+) transition at 1.1 eV, either of which results in the Cr(1+) being the stable charge state. Other prospective quantum defect centers might lurk undiscovered within GaN because they are not so straightforwardly available.

This pattern extends across the series. The vanadium lacks an acceptor level because the cost to disturb the triplet  $e$  doubleton pushes the V(1−) above the CBE. The Mn is an effective amphoteric dopant to create semi-insulating material because it is bounded by the widely stable  $d^5$  sextet at the top, creating a deep acceptor state, and the triplet  $e^2$  doubleton Mn(2+) at the bottom of the band gap stabilizing a deep double-donor state. For the Fe, the neutral sextet is predicted to be stable across a wide range of mid-gap Fermi levels, which pushed the (1−) state higher in the gap. The closed spin-shell (nearly?) stabilizes the triplet  $e$  doubleton for the Fe(3+). The Co(1−) quartet  $t_2$  tripleton is stable across the upper half of the gap, creating an acceptor level that pins the Fermi level even deeper than the Mn(1−/0) dopant. The crystal-field-stabilized closed shell  $e$  doubleton is the final donor state for Co at the bottom of the gap.

The defect level diagram depicted in Fig. 7 offers a full survey of what 3d dopant centers might exist and a sense of how they might be created. This diagram also offers a more quantitative understanding of how to engineer Fermi levels in GaN using 3d dopants. The prospect is that the search for new, potentially interesting quantum centers could rely less on serendipity and more upon intentional, quantitative understanding.

## VI. CONCLUSIONS

We have presented a systematic analysis of the structural, electronic, and optical properties of magnetic 3d dopants in cubic GaN using a local DFT functional in concert with a LMCC method for treating charged-supercell boundary conditions. The frequently stated objection to the use of the local DFT functional such as PBE, the notorious DFT band-gap problem, is shown to be unfounded for GaN. The computed spectrum of local defect charge transition energies solely con-

strained to just the charge states of 3d dopants is seen to span the experimental band gap. Predictions of the defect levels are seen to match those few levels observed in experiment (for Mn and Fe) as well or better than the results of hybrid functionals empirically tuned to reproduce the band gap. This lends credence to the predictions of defect levels across the entire 3d series. All the dopants, with the exception of V, are expected to be amphoteric, with most exhibiting a second donor charge state.

A second objection to use of local DFT functionals specific to 3d dopants had been their purported failure to yield a symmetry-lowering structural distortion in response to a Jahn-Teller-vulnerable degeneracy in Mn(0). We find these JT distortions to be present, although these are weaker in the smallest, least reliable supercells. These distortions are found to be present over the entire 3d series for all Jahn-Teller-susceptible, degenerate electronic states, with a sense (pairing or resonant  $D_{2d}$ ) consistent with available experiment. The sense of these distortions is shown to be related to  $e$ - and  $t_2$ -state occupations consistently across the series.

A slightly reduced accuracy appears to extend to predictions of the spin-forbidden transitions that can be computed from  $\Delta$ SCF from standard ground-state DFT calculations. The Mn, Fe, and Co each exhibit multiple spin states for multiple different charge states. This set of defects offers a rich environment to experimentally probe the boundary between the regime dominated by exchange coupling (favoring high spin, early in the 3d series) and the regime dominated by crystal-field splitting (driving the  $e$  shells below the high-spin coupled  $t_2$  orbitals, later in the series). The PBE calculations predict this boundary to occur later into the 3d series, into the Fe positive charge states, midway within the Co charge states, and to be complete in the later transition metals, as depicted in Fig. 11.

The single-particle energies from PBE also prove remarkably predictive of the spin-conserving excitations seen in experiment, providing additional support for those assignments and making predictions for potential transitions in other cases. These PBE calculations correctly predict the existence of intrasite  $d \rightarrow d$  transitions where hybrid functional calculations fail: the requisite occupied  $d$  states in hybrid functional calculations are buried far under the VBE [17]. The PBE results, however, appear to not completely escape this problem: while the spin-conserving excitation for the Mn(0) can manifest from an occupied  $e$  orbital right at the VBE, this single-particle orbital sinks below the VBE in the Mn(1+) and leaves no viable candidate for the 1.0-eV PL peak seen in experiment.

Even for the heavily studied case of Mn doping, there continue to be gaps in the understanding of defect properties. There still remains significant uncertainty in the interpretation of a large body of the experimental data for 3d dopants in GaN, and questions concerning the fundamental accuracy that might realistically be expected of the theory. The analysis in this paper suggests several directions to usefully probe important questions concerning the behavior and properties of 3d dopants, to test the limits and accuracy of the theory, thereby providing a useful framework to understand and interpret new results in the future.

## ACKNOWLEDGMENTS

We thank T. Wolfe (Air Force Institute of Technology) for useful discussions concerning the modeling of transition metal doping in semiconductors. Sandia National Laboratories is a multimission laboratory managed and operated by National Technology and Engineering Solutions of Sandia, LLC, a wholly owned subsidiary of Honeywell International, Inc., for the U.S. Department of Energy's National Nuclear Security Administration under Contract No. DE-NA0003525. This work (Sandia) was supported by a Laboratory Directed Research and Development (LDRD) project (No. 218242), and was funded, in part, at the Center for Integrated Nanotechnologies, an Office of Science User Facility operated for the U.S. Department of Energy (DOE) Office of Science. The information, data, or work presented herein was funded in part by the Advanced Research Projects Agency–Energy (ARPA-E), U.S. Department of Energy under the BREAKERS program directed by Dr. I. Kizilyalli. Air Force Research Laboratory gratefully acknowledges the support of the Air Force

Office of Scientific Research (AFOSR) through Contracts No. FA9550-17RVCOR505 and No. FA9550-21RVCOR503. This paper describes objective technical results and analysis. Any subjective views or opinions that might be expressed in the paper do not necessarily represent the views of the U.S. Department of Energy or the United States Government. This paper has been co-authored by employees of National Technology & Engineering Solutions of Sandia, LLC, under Contract No. DE-NA0003525 with the U.S. Department of Energy (DOE). The employees own all right, title, and interest in and to the article and are solely responsible for its contents. The United States Government retains and the publisher, by accepting the article for publication, acknowledges that the United States Government retains a nonexclusive, paid-up, irrevocable, world-wide license to publish or reproduce the published form of this article or allow others to do so, for United States Government purposes. The DOE will provide public access to these results of federally sponsored research in accordance with the DOE Public Access Plan [69].

- 
- [1] T. Dietl and H. Ohno, Dilute ferromagnetic semiconductors: Physics and spintronic structures, *Rev. Mod. Phys.* **86**, 187 (2014).
- [2] W. F. Koehl, B. Diler, S. J. Whiteley, A. Bourassa, N. T. Son, E. Janzén, and D. D. Awschalom, Resonant optical spectroscopy and coherent control of Cr<sup>4+</sup> spin ensembles in SiC and GaN, *Phys. Rev. B* **95**, 035207 (2017).
- [3] K. Gao, T. Aoki, M. Arita, Y. Arakawa, and M. Holmes, Observation of sharp emission lines from Zn-doped GaN, *Jpn. J. Appl. Phys.* **58**, SCCB15 (2019).
- [4] J. P. Perdew, K. Burke, and M. Ernzerhof, Generalized Gradient Approximation Made Simple, *Phys. Rev. Lett.* **77**, 3865 (1996).
- [5] M. A. Reshchikov and H. Morkoç, Luminescence properties of defects in GaN, *J. Appl. Phys.* **97**, 061301 (2005).
- [6] U. Gerstmann, A. T. Blumenau, and H. Overhof, Transition metal defect in group-III nitrides: An *ab initio* calculation of hyperfine interactions and optical transitions, *Phys. Rev. B* **63**, 075204 (2001).
- [7] L. Kronik, M. Jain, and J. R. Chelikowsky, Electronic structure and spin polarization of Mn<sub>x</sub> Ga<sub>1-x</sub> N, *Phys. Rev. B* **66**, 041203(R) (2002).
- [8] B. Sanyal, O. Bengone, and S. Mirbt, Electronic structure and magnetism of Mn-doped GaN, *Phys. Rev. B* **68**, 205210 (2003).
- [9] L. M. Sandratskii, P. Bruno, and J. Kudrnovsky, On-site Coulomb interaction and the magnetism of (GaMn)N and (GaMn)As, *Phys. Rev. B* **69**, 195203 (2004).
- [10] P. Boguslawski and J. Bernholc, Fermi-level effects on the electronic structure and magnetic couplings in (Ga,Mn)N, *Phys. Rev. B* **72**, 115208 (2005).
- [11] A. Wolos, A. Wyszomolek, M. Kaminska, A. Twardowski, M. Bockowski, I. Grzegory, S. Porowski, and M. Potemski, Neutral Mn acceptor in bulk GaN in high magnetic fields, *Phys. Rev. B* **70**, 245202 (2004).
- [12] M. Smolentsev, G. Smolentsev, S. Wei, and A. V. Soldatov, Local atomic structure around Mn ions in GaN:Mn thin films: Quantitative XANES analysis, *Phys. B (Amsterdam)* **406**, 2843 (2011).
- [13] X. Luo and R. M. Martin, Jahn-Teller distortion and ferromagnetism in the dilute magnetic semiconductors GaAs:Mn and cubic GaN:Mn, *Phys. Rev. B* **72**, 035212 (2005).
- [14] A. Stroppa and G. Kresse, Unraveling the Jahn-Teller effect in Mn-doped GaN using the Heyd-Scuseria-Ernzerhof hybrid functional, *Phys. Rev. B* **79**, 201201(R) (2009).
- [15] F. Viot, R. Hayn, and A. Boukourt, Electron structure and Jahn-Teller effect in GaN:Mn and ZnS:Cr, *J. Phys.: Condens. Matter* **23**, 025503 (2011).
- [16] O. Volnianska, T. Zakrzewski, and P. Boguslawski, Point defects as a test ground for the local density approximation +*U* theory: Mn, Fe, and *v*<sub>Ga</sub> in GaN, *J. Chem. Phys.* **141**, 114703 (2014).
- [17] T. Zakrzewski and P. Boguslawski, Electronic structure of transition metal ions in GaN and AlN: Comparing GGA+*U* with experiment, *J. Alloys Compd.* **664**, 565 (2016).
- [18] P. A. Schultz, SEQQUEST code, see <https://dft.sandia.gov/Quest/>
- [19] R. P. Messmer, B. McCarroll, and C. M. Singal, Molecular orbital approach to chemisorption: IV. LCAO band structures and the molecular unit cell., *J. Vac. Sci. Technol.* **9**, 891 (1972).
- [20] J. P. Perdew and A. Zunger, Self-interaction correction for density-functional approximations for many-electron systems, *Phys. Rev. B* **23**, 5048 (1981).
- [21] P. A. Schultz, Local electrostatic moments and periodic boundary conditions, *Phys. Rev. B* **60**, 1551 (1999).
- [22] P. A. Schultz, Charged Local Defects in Extended Systems, *Phys. Rev. Lett.* **84**, 1942 (2000).
- [23] P. A. Schultz, Theory of Defect Levels and the “Band Gap Problem” in Silicon, *Phys. Rev. Lett.* **96**, 246401 (2006).
- [24] P. A. Schultz and O. A. von Lillienfeld, Simple intrinsic defects in gallium arsenide, *Modelling Simul. Mater. Sci. Eng.* **17**, 084007 (2009).
- [25] P. A. Schultz, The *E1-E2* center in gallium arsenide is the divacancy, *J. Phys.: Condens. Matter* **27**, 075801 (2015).
- [26] M. Fuchs and M. Scheffler, *Ab initio* pseudopotentials for electron structure calculations of polyatomic systems using density functional theory, *Comput. Phys. Commun.* **119**, 67 (1999).

- [27] A. E. Mattsson, P. A. Schultz, M. P. Desjarlais, T. R. Mattsson, and K. Leung, Designing meaningful density functional theory calculations in materials science—a primer, *Model. Simul. Mater. Sci. Eng.* **13**, R1 (2005).
- [28] O. A. von Lilienfeld and P. A. Schultz, Structure and band gaps of Ga-(V) semiconductors: The challenge of Ga pseudopotentials, *Phys. Rev. B* **77**, 115202 (2008).
- [29] A. H. Edwards, P. A. Schultz, and R. M. Dobzynski, Electronic structure of intrinsic defects in c-gallium nitride: Density functional theory study without the jellium approximation, *Phys. Rev. B* **105**, 235110 (2022).
- [30] D. R. Hamann, Generalized norm-conserving pseudopotentials, *Phys. Rev. B* **40**, 2980 (1989).
- [31] T. S. Wolfe, R. M. Van Ginhoven, and A. Strachan, Computational study of first-row transition metals in monodoped 4H-SiC, *Modelling Simul. Mater. Sci. Eng.* **29**, 055008 (2021).
- [32] N. Troullier and J. L. Martins, Efficient pseudopotentials for plane-wave calculations, *Phys. Rev. B* **43**, 8861 (1991).
- [33] S. G. Louie, S. Froyen, and M. L. Cohen, Nonlinear ionic pseudopotentials in spin-density-functional calculations, *Phys. Rev. B* **26**, 1738 (1982).
- [34] P. A. Schultz, R. M. Van Ginhoven, and A. H. Edwards, Theoretical study of intrinsic defects in cubic silicon carbide 3C-SiC, *Phys. Rev. B* **103**, 195202 (2021).
- [35] L. J. Sham and W. Kohn, One-particle properties of an inhomogeneous interacting electron gas, *Phys. Rev.* **145**, 561 (1966).
- [36] P. A. Schultz, Discriminating a deep gallium antisite defect from shallow acceptors in GaAs using supercell calculations, *Phys. Rev. B* **93**, 125201 (2016).
- [37] P. A. Schultz and A. H. Edwards, Modeling charged defects inside density functional theory band gaps, *Nucl. Instrum. Methods B* **327**, 2 (2014).
- [38] G. Ramírez-Flores, H. Navarro-Contreras, A. Lastras-Martínez, R. C. Powell, and J. E. Greene, Temperature-dependent optical band gap of the metastable zinc-blende structure  $\beta$ -GaN, *Phys. Rev. B* **50**, 8433 (1994).
- [39] R. Dingle, D. D. Sell, S. E. Stokowski, and M. Ilegems, Absorption, reflectance, and luminescence of GaN epitaxial layers, *Phys. Rev. B* **4**, 1211 (1971).
- [40] C. G. Van de Walle and J. Neugebauer, First-principles calculations for defects and impurities: Applications to III-nitrides, *J. Appl. Phys.* **95**, 3851 (2004).
- [41] X. Y. Cui, B. Delley, A. J. Freeman, and C. Stampfl, Neutral and charged embedded clusters of Mn in doped GaN from first principles, *Phys. Rev. B* **76**, 045201 (2007).
- [42] T. Graf, M. Gjukic, L. Görgens, O. Ambacher, M. S. Brandt, and M. Stutzmann, Charge transfer at the Mn acceptor level in GaN, *J. Supercond.* **16**, 83 (2003).
- [43] R. Y. Korotkov, J. M. Gregie, and B. W. Wessels, Mn-related absorption and PL bands in GaN grown by metal organic vapor phase epitaxy, *Phys. B: Condens. Matter* **308-310**, 30 (2001).
- [44] A. Y. Polyakov, N. B. Smirnov, A. V. Govorkov, N. V. Pashkova, A. A. Shlensky, S. J. Pearton, M. E. Overberg, C. R. Abernathy, J. M. Zavada, and R. G. Wilson, Electrical and optical properties of Cr and Fe implanted *n*-GaN, *J. Appl. Phys.* **93**, 5388 (2003).
- [45] R. Y. Korotkov, J. M. Gregie, and B. W. Wessels, Optical properties of the deep Mn acceptor in GaN:Mn, *Appl. Phys. Lett.* **80**, 1731 (2002).
- [46] B. Han, B. W. Wessels, and M. P. Ulmer, Optical investigation of electronic states of Mn<sup>4+</sup> ions in *p*-type GaN, *Appl. Phys. Lett.* **86**, 042505 (2005).
- [47] D. O. Demchenko and M. A. Reshchikov, Blue luminescence and Zn acceptor in GaN, *Phys. Rev. B* **88**, 115204 (2013).
- [48] J. Baur, K. Maier, M. Kunzer, U. Kaufmann, and J. Schneider, Determination of the GaN/AlN band offset via the (-/0) acceptor level of iron, *Appl. Phys. Lett.* **65**, 2211 (1994).
- [49] R. Heitz, P. Maxim, L. Eckey, P. Thurian, A. Hoffmann, I. Broser, K. Pressel, and B. K. Meyer, Excited states of Fe<sup>3+</sup> in GaN, *Phys. Rev. B* **55**, 4382 (1997).
- [50] E. Malguth, A. Hoffmann, W. Gehlhoff, O. Gelhausen, M. R. Phillips, and X. Xu, Structural and electronic properties of Fe<sup>3+</sup> and Fe<sup>2+</sup> centers in GaN from optical and EPR experiments, *Phys. Rev. B* **74**, 165202 (2006).
- [51] P. Muret, J. Pernot, M. Azize, and Z. Bougrioua, Photoinduced current transient spectroscopy of deep levels and transport mechanisms in iron-doped GaN thin films grown by low pressure-metalorganic vapor metal epitaxy, *J. Appl. Phys.* **102**, 053701 (2007).
- [52] P. Alippi, F. Filippone, G. Mattioli, A. A. Bonapasta, and V. Fiorentini, Bound states of the Fe impurity in wurtzite GaN from hybrid density-functional calculations, *Phys. Rev. B* **84**, 033201 (2011).
- [53] Y. S. Puzyrev, R. D. Schrimpf, D. M. Fleetwood, and S. T. Pantelides, Role of Fe impurity complexes in the degradation of GaN/AlGaIn high-electron-mobility transistors, *Appl. Phys. Lett.* **106**, 053505 (2015).
- [54] D. Wickramaratne, J.-X. Shen, C. E. Dreyer, A. Alkauskas, and C. G. Van de Walle, Electrical and optical properties of iron in GaN, AlN, and InN, *Phys. Rev. B* **99**, 205202 (2019).
- [55] See Supplemental Materials at <http://link.aps.org/supplemental/10.1103/PhysRevB.107.205202> for detailed numerical tabulations of computed defect levels, neutral formation energies, and Jahn-Teller distortion energies.
- [56] J. Baur, K. Maier, M. Kunzer, U. Kaufmann, J. Schneider, H. Amano, I. Akasaki, T. Detchprohm, and K. Hiramatsu, Infrared luminescence of residual iron deep level acceptors in gallium nitride (GaN) epitaxial layers, *Appl. Phys. Lett.* **64**, 857 (1994).
- [57] J. Baur, U. Kaufman, M. Kunzer, J. Schneider, H. Amano, and K. Hiramatsu, Photoluminescence of residual transition metal impurities in GaN, *Appl. Phys. Lett.* **67**, 1140 (1995).
- [58] T. Devillers, M. Rovezzi, N. G. Szewacki, S. Dobkowska, W. Stefanowicz, D. Sztenkiel, A. Grois, J. Suffczyński, A. Navarro-Quezada, B. Faina, T. Li, P. Glatzel, F. d'Acapito, R. Jakiela, M. Sawicki, J. A. Majewski, T. Dietl, and A. Bonanni, Manipulating Mn-Mg<sub>k</sub> cation complexes to control the charge- and spin-state of Mn in GaN, *Sci. Rep.* **2**, 722 (2012).
- [59] B. Han, R. Y. Korotkov, B. W. Wessels, and M. P. Ulmer, Optical properties of Mn<sup>4+</sup> ions in GaN:Mn codoped with Mg acceptors, *Appl. Phys. Lett.* **84**, 5320 (2004).
- [60] K. Pressel, S. Nilsson, R. Heitz, A. Hoffman, and B. K. Meyer, Photoluminescence study of the 1.047 eV emission in GaN, *J. Appl. Phys.* **79**, 3214 (1996).
- [61] T. Dietl, F. Matsukura, and H. Ohno, Ferromagnetism of magnetic semiconductors: Zhang-Rice limit, *Phys. Rev. B* **66**, 033203 (2002).
- [62] W. Stefanowicz, D. Sztenkiel, B. Faina, A. Grois, M. Rovezzi, T. Devillers, F. d'Acapito, A. Navarro-Quezada, T. Li,

- R. Jakiela, M. Sawicki, T. Dietl, and A. Bonanni, Structural and paramagnetic properties of dilute  $\text{Ga}_{1-x}\text{Mn}_x\text{N}$ , *Phys. Rev. B* **81**, 235210 (2010).
- [63] A. Bonanni, M. Sawicki, T. Devillers, W. Stefanowicz, B. Faina, T. Li, T. E. Winkler, D. Sztenkiel, A. Navarro-Quezada, M. Rovezzi, R. Jakiela, A. Grois, M. Wegscheider, W. Jantsch, J. Suffczyński, F. D'Acapito, A. Meingast, G. Kothleitner, and T. Dietl, Experimental probing of exchange interactions between localized spins in the dilute magnetic insulator  $(\text{Ga,Mn})\text{N}$ , *Phys. Rev. B* **84**, 035206 (2011).
- [64] R. Nelson, T. Berlijn, J. Moreno, M. Jarrell, and W. Ku, What Is The Valence of Mn in  $\text{Ga}_{1-x}\text{Mn}_x\text{N}$ ? *Phys. Rev. Lett.* **115**, 197203 (2015).
- [65] A. Filippetti, N. A. Spaldin, and S. Sanvito, Self-interaction effects in  $(\text{Ga,Mn})\text{As}$  and  $(\text{Ga,Mn})\text{N}$ , *Chem. Phys.* **309**, 59 (2004).
- [66] H. Raebiger, S. Bae, C. Echeverría-Arrondo, and A. Ayuela, Control of hole localization in magnetic semiconductors by axial strain, *Phys. Rev. Mater.* **2**, 024402 (2018).
- [67] A. Zunger and U. Lindefelt, Substitutional  $3d$  impurities in silicon: A self-regulating system, *Solid State Comm.* **45**, 343 (1983).
- [68] A. Zunger, S. Lany, and H. Raebiger, The quest for dilute ferromagnetism in semiconductors: Guides and misguides by theory, *Physics* **3**, 53 (2010).
- [69] <https://www.energy.gov/downloads/doe-public-access-plan>.